



Interplay of acoustophoresis and dielectrophoresis in a standing surface acoustic wave field: from spherical to non-spherical particles

Sebastian Sachs¹ · David Schreier¹ · Felix Brand² · Klaus Stefan Drese² · Christian Cierpka¹ · Jörg König¹

Received: 2 July 2024 / Accepted: 26 August 2024
© The Author(s) 2024

Abstract

Standing surface acoustic waves (sSAW) emerged as a flexible tool for precise manipulation of spherical and non-spherical objects in Lab-on-a-Chip devices. While the manipulation of suspended particles and cells in acoustofluidic devices is mostly dominated by acoustic forces due to acoustic scattering and the acoustically induced fluid flow, surface acoustic waves are inherently linked to an inhomogeneous electric field. The superimposed effects of dielectrophoretic forces and torques on polarizable particles are less explored in microfluidics using sSAW. In this study, a thorough analysis of the physical interplay of acoustophoresis and dielectrophoresis aims to bridge this gap. In comprehensive experiments, the dielectrophoretic impact on the behavior of spherical and non-spherical particles is distinguished by screening the electric field of the sSAW inside the micro channel locally. As a result, particles are forced into trapping locations across the entire channel height. However, the height position close to the bottom differs between the screened and non-screened region. Regardless of the shape of the particles used in this study, particles are forced towards the bottom at the region with screening, while being levitated at regions without screening. This indicates clearly the influence of the electric field in close vicinity to the substrate surface. Furthermore, the unintuitive preferred orientation of prolate spheroids perpendicular to the pressure nodes of the sSAW recently reported, is confirmed in both region regardless of the presence of the electric field. Based on a three-dimensional numerical model, this orientation results not only due to the acoustic torque but is also caused by the dielectrophoretic torque, which complement each other. The experimental and numerical findings are in excellent agreement and provide deep insights into the underlying physical mechanisms responsible for patterning and orientation of the particles.

Keywords Surface acoustic waves · Acoustophoresis · Dielectrophoresis · Non-spherical particle · Acoustofluidics

1 Introduction

The systematic manipulation of microparticles and biological cells by acoustic wave fields developed into a flexible and scalable tool for Lab-on-a-Chip devices. With tailored acoustofluidic devices, a variety of applications for concentrating (Collins et al. 2016; Shilton et al. 2008), patterning (Shi et al. 2009; Deng et al. 2023), mixing (Ahmed et al. 2009; Zeng et al. 2011) and separating (Nam et al. 2011; Ding et al. 2014; Gao et al. 2020) of suspended particles

were demonstrated, which are highly relevant in pharmacy, chemistry and biomedical fields (Sajeesh and Sen 2014; Zhang et al. 2020; Miyagawa and Okada 2021). The key of acoustic particle manipulation as a non-invasive (Tian et al. 2020; Weser et al. 2022), label-free (Antfolk et al. 2015; Fan et al. 2022) and biocompatible (Wiklund 2012; Jiang et al. 2021) method is the targeted customizability of acoustic field patterns (Ding et al. 2013). In recent years, technologies based on surface acoustic waves (SAWs) emerged successfully. Corresponding devices are based on interdigital transducers (IDTs) to generate traveling or standing SAWs with wavelength λ_{SAW} on the surface of a piezoelectric substrate utilizing the inverse piezoelectric effect (Ding et al. 2013; Gao et al. 2020; Fan et al. 2022; Cheeke 2002). When the leaky SAWs encounter a fluid within a micro channel, part of their energy is radiated into the fluid and generates a longitudinal acoustic pressure wave. These acoustic waves propagate in the bulk of the fluid and are referred to as bulk

✉ Sebastian Sachs
sebastian.sachs@tu-ilmenau.de

¹ Institute of Thermodynamics and Fluid Mechanics,
Technische Universität Ilmenau, 98693 Ilmenau, Germany

² Coburg University of Applied Sciences and Arts,
ISAT - Institute of Sensor and Actuator Technology,
96450 Coburg, Germany

acoustic waves (BAW) in the following (Yeo and Friend 2014). Please note that the BAWs in this case are induced by leaky SAWs and not by the resonance of an acoustically hard fluid cavity, as is typical in BAW devices (Johnson and Feke 1995; Laurell et al. 2007; Leibacher et al. 2015). By superimposing two counter-propagating SAWs, a standing surface acoustic wave (sSAW) is formed, which gives rise to a pseudo-standing acoustic wave field with alternating pressure nodes and antinodes in the fluid domain (Barnkob et al. 2018). Simultaneously, the elastic surface deformations caused by the sSAW give rise to an electric potential due to the piezoelectric effect (Auld 1973). With the antinodes acting as virtual electrodes, an inhomogeneous electric field is formed in the fluid. Due to the superposition of the acoustic and electric field, suspended particles are exposed to an acoustoelectric wave field. The dynamic behavior of spherical particles is mainly determined by the interaction of the acoustic radiation force (King 1934; Bruus 2012), dielectrophoretic (DEP) force (Pohl and Crane 1972) and Stokes' drag (Çengel and Cimbala 2014) in these devices. The latter arises due to an acoustically induced fluid flow, which is driven by damping of the BAWs, the so-called acoustic streaming effect (Nyborg 1953). However, particles of non-spherical shape are further affected by the acoustic and dielectrophoretic torque, which pushes elongated particles into a stable orientation relative to the acoustic and electric field distribution (Fan et al. 2008; Silva et al. 2012; Wang et al. 1997).

Acoustic and dielectrophoretic forces have been used individually in many microfluidic devices to selectively separate spherical particles based on their size as well as mechanical and electrical properties (Gossett et al. 2010; Nasiri et al. 2020; Miyagawa and Okada 2021; Hettiarachchi et al. 2022). Furthermore, both forces were combined in a device using virtual deterministic lateral displacement to separate nanometer-sized particles by placing an IDT in a tilted alignment beneath a micro channel (Collins et al. 2014; Tayebi et al. 2021). Besides, the pattern formation of nanoparticles in a sessile droplet under the influence of the electric field of an sSAW was studied (Zheng et al. 2020). De Lora et al. (2024) examined the influence of acoustophoresis and dielectrophoresis on a thin film of surfactant molecules stabilizing a droplet emulsion. In a study by Ghayour et al. (Ghayour et al. 2018), DEP forces were used to trap cells between two IDTs, while the number of cells was detected by changes in the amplitude of an SAW. Zhang et al. (2021) developed an acoustoelectronic nanotweezer for manipulating sub-100 nm objects based on the influence of the electric field generated by a two-dimensional sSAW. The patterning and orientation of non-spherical particles in standing acoustoelectric wave fields were examined using carbon nanotubes (Strobl et al. 2004; Seemann et al. 2006; Zeng et al. 2013; Ma et al. 2015), chromium and insulated

silicon oxide tubes (Kong et al. 2010) as well as nanowires (Chen et al. 2013). However, the effect of the acoustic field on the behavior of non-spherical particles remains often the primary focus, while the influence of the electric field is neglected (Nam et al. 2011; Bernard et al. 2017; Wu et al. 2017; Richard et al. 2019; Gai et al. 2020; Sachs et al. 2023; Fakhfoury et al. 2023; Khan et al. 2024). Although the electric field is inherently linked to the sSAW, a thorough analysis of the physical interplay of acoustophoresis and dielectrophoresis in complex acoustofluidic devices is lacking.

This study aims to bridge this gap based on experimental and numerical investigations with spherical and non-spherical particles. The analyzed acoustoelectric wave field features several pressure nodes both along the channel height and width, as typically found in particle separation devices with e.g., tilted sSAWs (Ding et al. 2014; Li et al. 2015; Wu et al. 2017, 2018; Liu et al. 2019; Zhao et al. 2020). By designing the channel height to cover nearly three times the wavelength of the BAW, the exponential decay of the DEP force is exploited to create regions where either acoustophoresis or dielectrophoresis dominates. Here, $\lambda_{\text{BAW}} = \lambda_{\text{SAW}} c_0 / c_s$ is the wavelength of the BAW calculated by the speed of sound in the substrate c_s and fluid c_0 . Additionally, a thin metal layer was deposited below the micro channel and along half the aperture of the IDTs to screen the electric field. In this way, the influence of the electric field is revealed for spherical and non-spherical particles in the same device, which allows to elaborate the importance of the DEP force and torque. Based on the experimental findings, a three-dimensional numerical model was established that reveals the underlying acoustic and electric field quantities as well as forces and torques on both spherical and non-spherical particles.

The outline of the manuscript is as follows. In Sect. 2, the experimental and numerical methods applied are presented including a description of the acoustofluidic device. Subsequently, the observed behavior of spherical and non-spherical polystyrene particles in a pressure-driven micro flow is discussed in Sect. 3. The discussion is divided into experimental and numerical results. Finally, the paper brings the results to a conclusion. Please find also the electronic supplementary information (SI) with additional details on the numerical model and observations during experiments.

2 Methods

2.1 Acoustofluidic device

The acoustofluidic device comprises two opposing IDTs, which are deposited on a piezoelectric substrate made of 128° YX LiNbO₃ with a thickness of 500 μm (see Fig. 1).

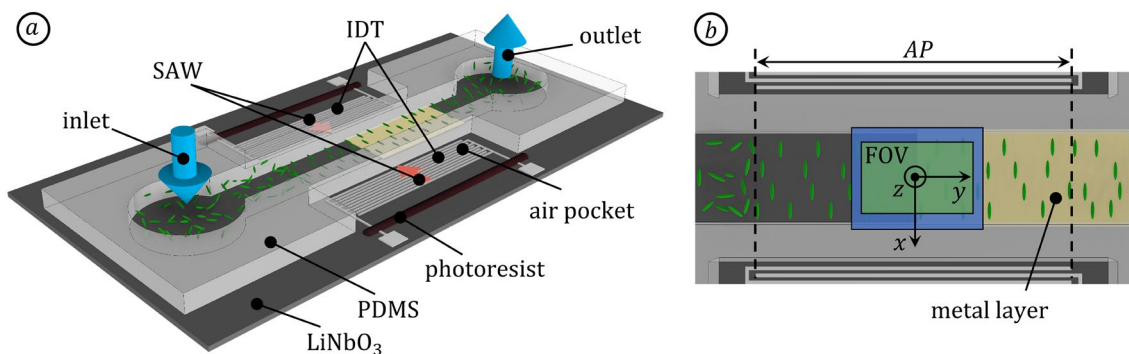


Fig. 1 Schematic of the acoustofluidic device with prolate spheroids (green) (a). Sealing of the micro channel was achieved by a PDMS cover, which is not visualized. The thin metal layer (gold) as well as

the FOV in experiments with spherical and non-spherical particles are displayed in blue and green, respectively, from a top view in (b) (color figure online)

The IDTs feature an aperture of $AP = 2 \text{ mm}$ and consist of 33 pairs of finger electrodes made of a 5 nm titanium layer as adhesion promoter and a 295 nm thick aluminum layer. The width and spacing of the finger electrodes amounts to one quarter of the wavelength of the SAW $\lambda_{\text{SAW}} = 150 \mu\text{m}$. A passivation layer of 385 nm silicon dioxide (SiO_2) serves to protect against corrosion and mechanical damage. Since excited SAWs propagate to both sides of the bidirectional IDTs, a layer of photoresist was applied to the substrate surface to completely attenuate the outward traveling waves. A thin metal layer (10/10 nm Cr/Au, see Fig. 1) covered the substrate surface beneath the fluid channel along half the aperture of the IDTs to screen the electric field of the SAW locally.

A straight micro channel with a cross-section of $500 \times 180 \mu\text{m}^2$, which corresponds to a channel height of about $2.86\lambda_{\text{BAW}}$, made of polydimethylsiloxane (PDMS) enclosed a particle suspension centrally between the IDTs. Sealing of the fluid domain is achieved by adhesion between the PDMS and the SiO_2 -covered LiNbO_3 substrate. Due to air pockets in the region of the IDTs, the thickness of the channel side walls is reduced to approx. $500 \mu\text{m}$ to limit the attenuation of the SAWs. Using a glass syringe ($500 \mu\text{L}$, ILS Innovative Laborsysteme GmbH) and a syringe pump (neMESYS, cetoni GmbH), the particle suspension was pumped through the micro channel with a pulsation-free volume flow rate of $Q = 1 \mu\text{L min}^{-1}$.

2.2 Experimental procedure

Experiments were conducted with fluorescent spherical polystyrene particles (PS-FluoRed, radius $R = 2.52 \mu\text{m}$, Ex/Em 530 nm/607 nm, MicroParticles GmbH) and prolate spheroids. Since the prolate spheroids were prepared based on the spherical particles in a stretching process, they possess the same volume. Details on the preparation of the non-spherical particles can be found in Weirauch

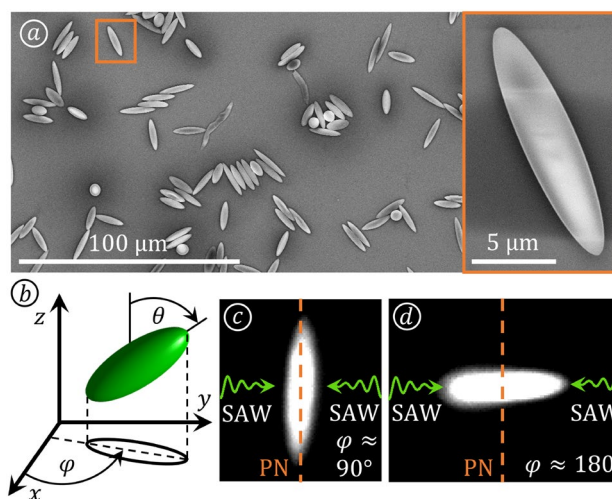


Fig. 2 SEM image of prolate spheroids dried on a silicon wafer (a) with a detailed view on one particle (marked by an orange frame) as inset. The coordinate system for the spatial position (x, y, z) and orientation (φ, θ) of the non-spherical particles is given in (b) and has been adapted from Sachs et al. (2023). A particle at $\varphi \approx 90^\circ$ or 270° (c) and $\varphi \approx 0^\circ$ or 180° (d) is oriented parallel and perpendicular to the pressure nodes, respectively (color figure online)

et al. (2022). In Fig. 2a, prolate spheroids dried off on a polished silicon wafer are depicted in a scanning electron microscopy (SEM) image. Due to the stretching process, the particles show a rather broad distribution in the aspect ratio $\Gamma = a_{\text{major}}/a_{\text{minor}}$ around the mean value of 4.1 (Sachs et al. 2023). Here, a_{major} and a_{minor} are the length of the major and minor axis, respectively. To reveal the behavior of the particles in the acoustoelectric wave field, they were suspended at a concentration below $9.6 \times 10^6 \text{ mL}^{-1}$ in either deionized water or aqueous glycerol solution (24% v/v). Prior to the experiments, 0.2% (v/v) polysorbate 80 (Biorigin) was added to the fluids and the micro channel

was flushed with isopropanol and the respective fluid. In this way, the risk of air bubbles, particles adhering to the channel margins and particle agglomeration was reduced.

To measure the spatial positions (x, y, z) of the spherical particles, an astigmatism particle tracking velocimetry (APTV) (Cierpka et al. 2010) setup similar to the arrangement in König et al. (2020) was used. Briefly, the acoustofluidic device was mounted on top of an inverted microscope (Axio Observer 7, Zeiss GmbH) with a Plan-Neofluar objective (M20X, NA = 0.4, Zeiss GmbH). The particles were illuminated by a modulatable OPAL laser ($\lambda_{\text{LASER}} = 532 \text{ nm}$, $P_{\text{LASER,max}} = 8 \text{ W}$, tarm laser technologies tlt GmbH & Co. KG), and the fluorescence signal was separated using a dichroic mirror (DMLP567T, Thorlabs Inc) and a long pass filter (FELH0550, Thorlabs Inc). Since the optical access was realized from below through the birefringent LiNbO_3 substrate, an additional linear polarization filter was placed in the optical path (Kiebert et al. 2017). The suspended particles were captured in double frame images with a defined time interval using an sCMOS camera (imager sCMOS, LaVision GmbH, 16 bit, 2560×2160 pixel). Due to a cylindrical lens (focal length 250 mm) located approx. 40 mm in front of the camera, the images of the spherical particles appear elliptically distorted. The experiments were divided into several measurement runs. To remove adhering particles and particle agglomerations, the micro channel was flushed between the measurement runs without exciting the sSAW. The individual measurements were started 6 s after switching on the sSAW to reach steady state. In order to cover the entire channel height, the measurement volume was traversed in $\Delta z/n = 10 \mu\text{m}$ steps along the z -axis. Here, n denotes the refractive index of the fluid. In each measurement plane, at least 900 double frame images were recorded at a frame rate of 10 Hz.

The field of view (FOV) was located in the center of the aperture between the two IDTs and covered the entire channel width and approx. $800 \mu\text{m}$ in main flow direction (y , see Fig. 1b). The regions of free and metallized substrate surface were each captured in one half of the image. A background subtraction and a Gaussian filter with a kernel size of 5×5 pixel were used to pre-process the images. As a consequence of the observation through the thin metal layer, the intensity signal and signal-to-noise ratio of the particle images was reduced in the metallized region. For this reason, the segmentation and identification of the particle images based on a threshold in intensity was performed separately for both regions. By fitting one-dimensional Gaussian functions in x - and y -direction, subpixel accuracy was achieved in the determination of the in-plane position (x, y) and length of the semi-axes (a_x, a_y) of the elliptically distorted particle images (Kähler et al. 2012). The depth position of the particles was found by mapping the particle

shape (a_x, a_y) to z using the Euclidean distance to a calibration function determined beforehand (Cierpka et al. 2011). In a quantitative analysis, the relative measurement error in the depth position was found to be below 3% (Barnkob et al. 2021). Detected particles were considered valid if the Euclidean distance between the particle and calibration function in the $a_x a_y$ -plane was less than 2 or 5 pixel in the region of free or metallized substrate surface, respectively. The displacement vector \mathbf{d} was determined by tracking the particles in the double frame images with a simple nearest-neighbor algorithm (Cierpka et al. 2013). Adhering particles with $|\mathbf{d}| < 0.25$ pixel were not considered in the further analysis.

While the behavior of the spherical particles is described by the spatial position (x, y, z) , the prolate spheroids are further characterized by the in-plane and out-of-plane orientation (φ, θ) (see Fig. 2b). As illustrated in Fig. 2c, a prolate spheroid at $\varphi = 90^\circ$ or 270° is oriented parallel to the pressure nodes. Vice versa, a particle at $\varphi = 0^\circ$ or 180° is oriented in line with the propagating SAW or perpendicular to the pressure nodes of the acoustoelectric wave field (see Fig. 2d). The suspended prolate spheroids were captured by following the same experimental procedure, but without a cylindrical lens in front of the camera. In this case, the FOV spanned $457 \times 542 \mu\text{m}^2$ in the xy -plane (see Fig. 1b). To determine the in-plane positions (x, y) and orientations (φ) of the non-spherical particles, the algorithm developed by Sachs et al. (2023) was used. However, an additional outlier filter based on the ratio of the summed intensities $I_{\text{sum}}/(I_{\text{ex}} - I_{\text{sum}})$ was added to reject strongly defocused particle images. Here, I_{sum} refers to the summed intensity within the detected particle contour and I_{ex} to a particle contour extended by a factor of 1.25. A similar approach was employed in previous studies to exclude overlapping particle images (Franchini and Krevor 2020; Sachs et al. 2023; Ratz et al. 2023). An uncertainty estimation based on synthetic particle images revealed subpixel accuracy in the determination of the x - and y -positions of the particles as well as a mean absolute error of 0.03° for the in-plane angle φ (Sachs et al. 2023). Since no APTV was applied for the non-spherical particles, an estimation of the particle distribution along the z -direction is obtained from the number of particles detected in the measurement planes ($\Delta z/n = 5 \mu\text{m}$), although the z -position of the particles was not determined. While the in-plane angle φ could be determined reliably, the out-of-plane angle θ could not be measured during the experiments. Readers who are interested in the measurement of the out-of-plane angle are referred to Sachs et al. (2023).

2.3 Measurement of the SAW amplitude

A thin metal layer was deposited on the substrate surface across half the aperture of the IDTs to introduce a screening effect of the electric field. However, the metal layer also slightly changes the phase velocity of the SAW (Weser et al. 2020). To investigate the influence of the metallization on the amplitude of the SAW, the normal displacement component of the substrate surface was measured using an ultra-high frequency laser Doppler vibrometer (LDV, UHF-120, Polytec GmbH). In the measurement, an AC voltage of frequency $f = 25.73$ MHz was applied to one IDT while the opposite IDT was covered by photoresist. Optical access to the substrate surface was provided from above by excluding the micro channel. Hence, an influence of the channel side walls on the amplitude of the SAW due to diffraction and damping was neglected in the measurement (Weser et al. 2020, 2022). The amplitude of the generated travelling SAW was measured pointwisely ($\Delta y = 10 \mu\text{m}$, duration 1 ms) along three lines with a distance $\Delta x = 10 \mu\text{m}$ parallel to the aperture. After averaging between the three lines, only a marginal influence of the metal layer on the mean amplitude of the SAW was evident (see Fig. S1, SI). Hence, similar acoustic fields are assumed in both regions of the micro channel. Based on the measured amplitude of the SAW, a comparison with numerical results is provided in the SI.

2.4 Numerical simulation

The three-dimensional acoustoelectric wave field was calculated numerically in two steps. In the first step, the propagation and superposition of the SAWs in the LiNbO₃ substrate was resolved. The numerical model includes the piezoelectric substrate with 20 pairs of electrodes representing one IDT as well as the fluid and PDMS domains as depicted in Fig. S2 (SI). To limit the numerical effort, a symmetry condition was set at $x/\lambda_{\text{SAW}} = 0$, modeling only half of the acoustofluidic device. The electromechanical coupling in the piezoelectric substrate is governed by the constitutive equations (Auld 1973)

$$\begin{bmatrix} \mathbf{T} \\ \mathbf{D} \end{bmatrix} = \begin{bmatrix} \mathbf{c} & -\mathbf{e} \\ \mathbf{e} & \epsilon_0 \epsilon_r \end{bmatrix} \begin{bmatrix} \mathbf{S} \\ \mathbf{E} \end{bmatrix}, \tag{1}$$

including the stress tensor \mathbf{T} , the electric displacement vector \mathbf{D} , the linearized strain tensor $\mathbf{S} = (\nabla \mathbf{u} + (\nabla \mathbf{u})^T)/2$ utilizing the mechanical displacement \mathbf{u} and the electric field \mathbf{E} . Furthermore, the elasticity tensor, piezoelectric tensor, electrical permittivity of vacuum and relative permittivity tensor of the substrate are expressed by \mathbf{c} , \mathbf{e} , ϵ_0 and ϵ_r , respectively. Applying the quasi-static assumption, the electric field is irrotational, i.e., $\nabla \times \mathbf{E} = 0$, and can be considered as a gradient $\mathbf{E} = -\nabla \phi$ of the scalar electric

potential field ϕ (Hsu and Chao 2020). In the absence of free charges, the mechanical and electrical displacement (\mathbf{u} , \mathbf{D}) are determined by

$$\nabla \cdot \mathbf{T} = \rho_s \ddot{\mathbf{u}}, \tag{2}$$

$$\nabla \cdot \mathbf{D} = 0, \tag{3}$$

where the density of the LiNbO₃ substrate is given by ρ_s (Auld 1973; Hsu and Chao 2020). All material properties of 128° YX LiNbO₃ used in the simulation are listed in Tab. S1 with a tensor rotation applied.

The mechanical and electrical energy of the SAW couples into the PDMS and fluid domain of the micro channel. Simultaneously, repercussions on the mechanical displacement and electric potential at the substrate surface occur, which result in an attenuation of the SAW. Within the PDMS and fluid domain, the electrostatic field \mathbf{E} is characterized by Gauss’s law (Riccardi and Martin 2023; Zhang et al. 2021)

$$\nabla \cdot (\epsilon_0 \epsilon_{r,0} \mathbf{E}) = \rho_v, \tag{4}$$

$$\mathbf{E} = -\nabla \phi, \tag{5}$$

utilizing the space charge density ρ_v and relative permittivity of the fluid $\epsilon_{r,0}$. To reduce the numerical effort, the acoustic fields were calculated solely in the fluid domain. This approach is based on the modeling of fluid-PDMS interfaces by impedance boundary conditions. Furthermore, the attenuation of the SAW by the channel side walls was treated as an offset in the SAW amplitude. Applying the well-known perturbation theory (Bruus 2012) and neglecting viscous boundary layers, the acoustic pressure p_1 and acoustic velocity \mathbf{v}_1 in the fluid bulk are determined as first-order quantities by (Joergensen and Bruus 2021; Joergensen 2022)

$$\nabla^2 p_1 = -k_c^2 p_1, \tag{6}$$

$$\mathbf{v}_1 = -\nabla \left[\frac{i + \Gamma_s}{\omega \rho_0} p_1 \right], \tag{7}$$

$$k_c = \frac{\omega}{c_0} (1 + i\Gamma_{\text{total}}), \tag{8}$$

$$\Gamma_{\text{total}} = \frac{\omega}{2c_0^2 \rho_0} \left[(1 + \beta)\mu_0 + (\gamma - 1) \frac{k_0^{th}}{C_{p,0}} \right], \tag{9}$$

$$\Gamma_s = \frac{(1 + \beta)\omega \mu_0}{2c_0^2 \rho_0}, \tag{10}$$

where k_c , $\omega = 2\pi f$, $\beta = \mu_b/\mu_0 + 1/3$ and $\gamma = C_{p,0}/C_{v,0}$ refer to the complex wave number, angular frequency, viscosity ratio and ratio of specific heat capacities, respectively. Furthermore, the density ρ_0 , speed of sound c_0 , thermal conductivity k_0^{th} and specific heat capacities at constant pressure $C_{p,0}$ and volume $C_{v,0}$ of the undisturbed fluid are used to specify the viscous and total damping coefficients Γ_s and Γ_{total} , respectively. Numerical calculations were performed in the frequency domain, since a harmonic time-dependence with the excitation frequency f is assumed for both the acoustic and electric field quantities. For greater detail and validation of the numerical model, the interested reader is referred to our previous study (Sachs et al. 2023), where the numerical model was used for a similar device.

Based on the simulation, the normal surface displacement and the electric potential were known at the substrate surface. These field quantities served as boundary conditions in the second step, in which the acoustic and electric fields within the fluid were calculated in separate reduced models as illustrated in Fig. S3 (SI). In this way, a decoupled calculation was achieved with less resources required. Hence, parameter studies were enabled since the wave propagation in the substrate did not have to be recalculated based on the full model. The reduced model for calculating the electric field quantities based on Eqs. (4) and (5) comprises the PDMS and fluid domains. In turn, the reduced model for the acoustic field quantities only includes the fluid domain (Sachs et al. 2023). However, the fluid velocity v_2 and pressure p_2 of the acoustically induced flow were further calculated as second-order quantities according to (Riaud et al. 2017; Bach and Bruus 2018)

$$0 = \nabla \cdot \langle v_2 \rangle, \quad (11)$$

$$0 = -\langle \nabla p_2 \rangle + \mu_0 \nabla^2 \langle v_2 \rangle + f_{ac}, \quad (12)$$

$$f_{ac} = \frac{1}{4} \nabla (\kappa_0 |p_1|^2 - \rho_0 |v_1|^2) + \frac{2\Gamma_s \omega}{c_0^2} \langle p_1 v_1 \rangle. \quad (13)$$

Here, the first two terms of the acoustic body force f_{ac} are absorbed in the excess pressure $\tilde{p}_2 = p_2 - 1/4(\kappa_0 |p_1|^2 - \rho_0 |v_1|^2)$ (Riaud et al. 2017), while the isentropic compressibility of the undisturbed fluid is given by $\kappa_0 = 1/(\rho_0 c_0^2)$. The applied boundary conditions of all models, material properties and a mesh independence study (see Fig. S4) can be found in the SI.

The time-averaged dielectrophoretic force F_{DEP}^s , acoustic radiation force F_{RAD} and drag force F_{DRAG} on a compressible spherical particle with $R \ll \lambda_{SAW}$ in a standing acoustoelectric wave field were calculated by (Pohl and Crane 1972; Bach and Bruus 2020)

$$F_{DEP}^s = -\nabla \xi, \quad (14)$$

$$F_{RAD} = -\nabla U, \quad (15)$$

$$F_{DRAG} = 6\pi\mu_0 R(v_2 - v_p), \quad (16)$$

$$\xi = -2\pi R^3 \epsilon_0 \epsilon_{r,0} CM^r |E_{rms}|^2, \quad (17)$$

$$U = \frac{2\pi R^3}{3} \left[\frac{\kappa_0 f_1^{rr}}{2} \langle |p_1|^2 \rangle - \frac{3\rho_0 f_2^{rr}}{4} \langle |v_1|^2 \rangle \right], \quad (18)$$

using the dielectrophoretic force potential ξ and Gor'kov potential U . The monopole and dipole scattering coefficients (f_1, f_2) were calculated according to Settnes and Bruus (2012), while the real part of a quantity is denoted by the superscript r . Details on the calculation of the Clausius-Mossotti factor CM can be found in Tayebi et al. (2021). However, since the real part of the Clausius-Mossotti factor is negative, the DEP force is acting to push the particles away from the charged surface of the piezoelectric substrate (Morgan et al. 2003). Furthermore, the root-mean-square value of the electric field is denoted by E_{rms} and the particle velocity by v_p . The three forces ($F_{DEP}^s, F_{RAD}, F_{DRAG}$) acting on a polystyrene particle with $R = 2.52 \mu\text{m}$ suspended in the fluid-filled micro channel typically reach peak values in the sub-nanonewton range at a peak-to-peak voltage of 20 V applied to the IDTs. However, due to the spatial pattern of F_{RAD} and F_{DRAG} , the motion of the particle is dominated by F_{DEP}^s near the channel bottom. As F_{DEP}^s decreases exponentially with the distance to the substrate surface, F_{RAD} and F_{DRAG} gain significance at higher z -levels.

To describe the behavior of non-spherical particles in the acoustoelectric wave field numerically, a prolate spheroid was modeled as an elastic solid domain in the fluid. The displacement field u_s within the solid domain is determined by the divergence of the stress tensor σ_s according to (Skov and Bruus 2016; Hoque et al. 2022)

$$\nabla \cdot \sigma_s + \rho_p \omega^2 u_s = 0, \quad (19)$$

$$\sigma_s = \rho_p [c_{PS,s}^2 (\nabla u_s + (\nabla u_s)^T) + (c_{PS,p}^2 - 2c_{PS,s}^2) (\nabla \cdot u_s) \mathbf{I}], \quad (20)$$

where the density, pressure wave speed and shear wave speed of the polystyrene particle are denoted by $\rho_p, c_{PS,p}$ and $c_{PS,s}$, respectively. The unit tensor refers to \mathbf{I} . Repercussions of the suspended particle on the acoustic fields were considered by coupling the calculation in the fluid and solid domain via an acoustic-structure boundary condition at the particle surface. The time-averaged acoustic and dielectrophoretic force (F_{AC}, F_{DEP}) and torque (T_{AC}, T_{DEP}) on the prolate spheroid

were determined by integrating over the particle equilibrium surface S_0 according to (Wang et al. 1997; Doinikov 1997; Karlsen 2018; Dual et al. 2012)

$$F_{AC} = \int_{S_0} \left[\langle \sigma_2 \rangle - \rho_0 \langle v_1 v_1 \rangle \right] \cdot n \, dS, \tag{21}$$

$$F_{DEP} = \int_{S_0} \langle \tau \rangle \cdot n \, dS, \tag{22}$$

$$T_{AC} = \int_{S_0} r \times \left[\langle \sigma_2 \rangle - \rho_0 \langle v_1 v_1 \rangle \right] \cdot n \, dS, \tag{23}$$

$$T_{DEP} = \int_{S_0} r \times (\langle \tau \rangle \cdot n) \, dS. \tag{24}$$

Here, n refers to the outward pointing normal vector at S_0 and r to a vector pointing from the center of mass to S_0 . The acoustic force and torque comprises the momentum flux tensor $\rho_0 \langle v_1 v_1 \rangle$ and hydrodynamic effects due to the acoustically induced fluid flow based on the second-order stress tensor $\sigma_2 = -p_2 I + \mu_0 [\nabla v_2 + (\nabla v_2)^T]$. Contributions resulting from electromagnetism were neglected in the Maxwell stress tensor $\tau = \epsilon_0 \epsilon_r \epsilon_0 (EE - 1/2 |E|^2 I)$ (Riccardi and Martin 2023). All numerical calculations were carried out using Comsol Multiphysics® (version 6.1, Comsol multiphysics 2024) as described in detail in the SI.

3 Results and discussion

3.1 Physical description

The physical mechanisms underlying the observed particle behavior are examined using the acoustofluidic device described in Sect. 2.1. By connecting the IDTs to an alternating voltage of resonant frequency $f = 25.7$ MHz (PowerSAW generator, Belektronik GmbH), counter-propagating SAWs of wavelength $\lambda_{SAW} = 150 \mu\text{m}$ are excited due to the inverse piezoelectric effect (Cheeke 2002). The excited SAWs propagate in Rayleigh mode along the crystallographic X-axis of the LiNbO₃ substrate and superimpose between both IDTs. The resulting sSAW features several periodically arranged nodes and antinodes at the substrate-fluid interface. The elastic surface deformations caused by the sSAW in turn generate an electrical potential due to the piezoelectric effect. Hence, the sSAW is inherently accompanied by an alternating electric field of same frequency.

The SAWs are attenuated as they propagate beneath the micro channel, while part of their energy is radiated into the

PDMS and fluid to form BAWs. The wavelength of the BAW in water and aqueous glycerol solution (24 % v/v) amounts to $\lambda_{BAW} = 58.2 \mu\text{m}$ and $62.9 \mu\text{m}$, respectively. Due to the small Rayleigh angle and the strong damping of the BAWs propagating in the PDMS (Kiebert et al. 2017; Barnkob et al. 2018), the BAWs directly coupled into the fluid provide the main source to generate a pseudo-standing wave field. The resulting pseudo-standing wave field contains standing and traveling wave components both along the channel width due to the attenuation of the SAWs and along the channel height due to partial reflection of the BAWs at the fluid-PDMS interfaces. As a result of viscous damping of the BAWs in the fluid and gradients in the pressure field, a stationary fluid flow is induced by the so-called acoustic streaming effect (Nyborg 1953). In addition, the electric field accompanying the sSAW expands into the fluid with field lines connected between neighboring antinodes of the sSAW. Due to the periodic pattern of the sSAW, an inhomogeneous electric field is formed in the fluid bulk.

A polarizable particle with non-zero acoustic contrast factor is predominantly affected by the acoustic radiation force due to wave scattering (King 1934), Stokes' drag due to the fluid flow and the DEP force due to induced di- or multipoles in the particle and the surrounding fluid (Nili et al. 2011). The motion of suspended particles is thus influenced by both, acoustophoresis and dielectrophoresis. To differentiate between these effects experimentally, two measures were adopted. First, the channel height was chosen large enough to cover several pressure nodes in the vertical direction. In this way, a region exists in which the particle motion is dominated by acoustophoresis, since the magnitude of the electric field decays exponentially with the distance to the substrate (Collins et al. 2014) whereas the acoustic field is present in the whole channel with similar amplitude. Second, the substrate-fluid interface was partly covered by a thin metal layer, dividing the micro channel in two regions with a free and metallized substrate surface (see Fig. 1). While the metal layer largely screens the electric field, the amplitude of the sSAW is affected only marginally (see Sect. 2.3). Consequently, the DEP force is greatly reduced in the region above the metallized substrate surface. A comparison of the particle behavior above the free and metallized substrate surface thus reveals the interplay of acoustophoresis and dielectrophoresis.

3.2 Dynamical behavior of spherical particles

Experiment The dynamical behavior of spherical polystyrene particles with radius $R \ll \lambda_{SAW}$ suspended in a pressure-driven micro flow was initially analyzed without the influence of the acoustoelectric wave field. The particles passed through a region with free ($y/AP < 0$) and metallized

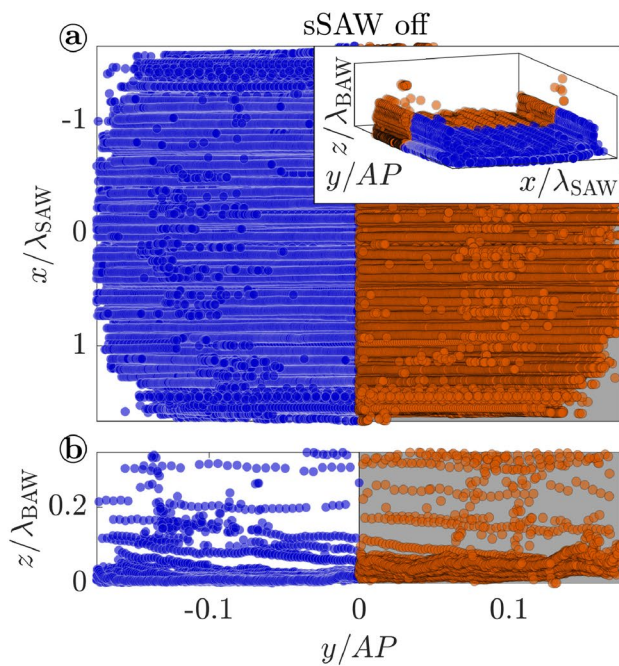
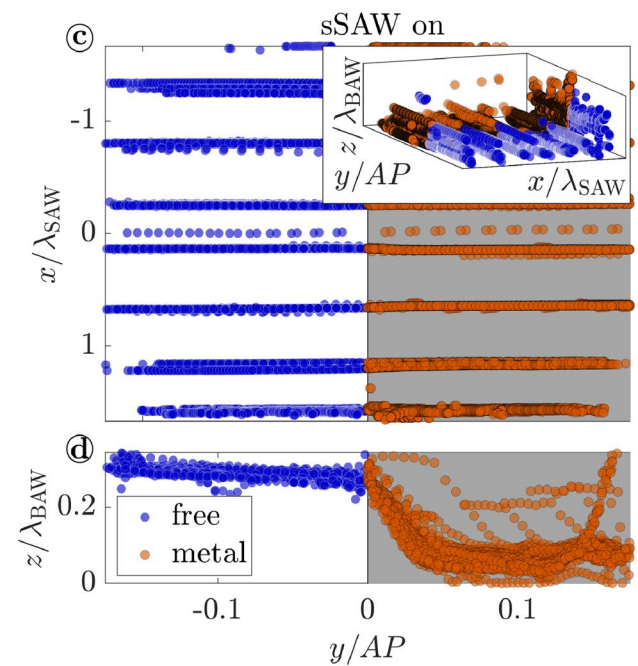


Fig. 3 Spherical particles with $R = 2.52 \mu\text{m}$ in a pressure-driven flow of deionized water, detected by applying APTV without sSAW (**a, b**) and with sSAW (**c, d**, $P_{\text{el}} = 50.9 \text{ mW}$). Particles located in regions above the free and metallized substrate surface are highlighted in blue on a white background and orange on a gray background, respectively. The entire channel width is covered in (**a, c**) from the top view,

($y/AP > 0$) substrate surface, as depicted by the detected particle positions in Fig. 3 in blue and orange, respectively. An uniform particle distribution was present across the channel width. However, the particles were predominantly found near the channel floor as a result of sedimentation (see Fig. 3b), since the density of the particles ρ_p was greater than that of the fluid ρ_0 . Only in the vicinity of the channel side walls, particles were located in higher positions. This phenomenon is caused by complementary effects of sedimentation in the inlet tube and flow diversion at the channel inlet as well as slower sedimentation near vertical walls (Farzam Rad and Moradi 2020; Yazdi and D'Avino 2023).

As soon as the sSAW was excited, the particles were focused on stable x -locations with a distance of approx. $\lambda_{\text{SAW}}/2$ along the channel width (see Fig. 3c). However, no significant variation of the lateral particle positions appeared between particles located in the region of free or metallized substrate surface. Since the dielectrophoretic force on the spherical particles F_{DEP}^s was strongly reduced in the metallized region, the lateral focusing of the particles was thus dominated by acoustic forces, as discussed further below based on numerical calculations. Similar to the particle distribution without sSAW, the particles were located near the channel floor. However, the particles with negative CM' were levitated by approx. $14 \mu\text{m}$ or



while three-dimensional views are added as insets. In (**b, d**), particles detected close to the channel floor are depicted at $x/\lambda_{\text{SAW}} \in [0, 1/3]$. Please note that the scale of the abscissa in (**b, d**) also applies to (**a, b**) and the legend in (**d**) to all subplots (color figure online)

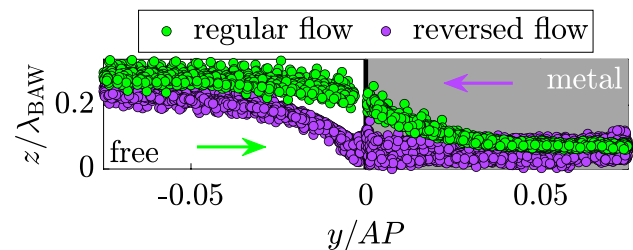


Fig. 4 Measured particle locations near the channel floor under the influence of the acoustoelectric field with $P_{\text{el}} \approx 30.5 \text{ mW}$. Detected particles highlighted in green were suspended in a main flow directed in positive y -direction (regular flow), while particles marked in purple flowed in negative y -direction (reversed flow) as highlighted by arrows. To distinguish particles focused to stable locations, a nearest neighbour filter was applied, where detected particles with less than 40 particles in an Euclidean distance less than $5 \mu\text{m}$ were rejected (color figure online)

$z/\lambda_{\text{BAW}} \approx 0.22$ above the free substrate surface, as indicated in Fig. 3d by detected particles at $x/\lambda_{\text{SAW}} \in [0, 1/3]$. As soon as the particles entered the region with the metallized substrate surface, the majority was pushed downwards. This vertical displacement occurred faster than that by sedimentation in Fig. 3b due to the effect of the acoustic force and the greatly reduced dielectrophoretic force.

In particular, the particles were pushed towards the channel floor directly after reaching the metallized substrate surface. This effect occurred similarly when reducing the electrical power applied to the IDTs from about 50.9 mW to 30.5 mW as depicted in Fig. 4. Furthermore, no differences were found by reversing the main flow direction. Again, particles were located in direct vicinity of the channel floor in the metallized region, but were levitated by F_{DEP}^s in the region of free substrate surface (see Fig. 4). Since strong gradients in y -direction are present in the electric field and dielectrophoretic force potential ξ above the edge of the thin metal layer ($y/AP = 0$), particles tend to agglomerate locally if the dielectrophoretic force component $F_{DEP,y}^s$ exceeds the Stokes' drag $F_{DRAG,y}$. This effect is shown numerically in Fig. S5 and experimentally in Fig. S6 (SI) for spherical as well as in video S2 (SI) for non-spherical particles. In tailored acoustofluidic devices, this behavior can be used for sequential particle concentration or separation, as demonstrated by Giesler et al. (2023) based on a device using interdigitated electrodes.

In order to investigate the behavior of suspended particles across the entire channel height, an aqueous glycerol solution (24% v/v) with a density $\rho_0 \approx 1.067 \text{ g/cm}^3$ higher than that of the particles ($\rho_p = 1.050 \text{ g/cm}^3$) was utilized in the following. Due to the density mismatch, particles were located mainly in the upper region of the micro channel when no sSAW was excited (see Fig. 5a). By exciting the sSAW, the spherical particles were focused on stable locations in three planes along the channel height: Near the channel floor, in the fluid bulk and near the channel ceiling (see Fig 5b). In accordance with prior observations, there was no significant influence of the thin metal layer on the lateral positions of the focused particles regardless of their height position. Although only 0.1 % of the detected particles

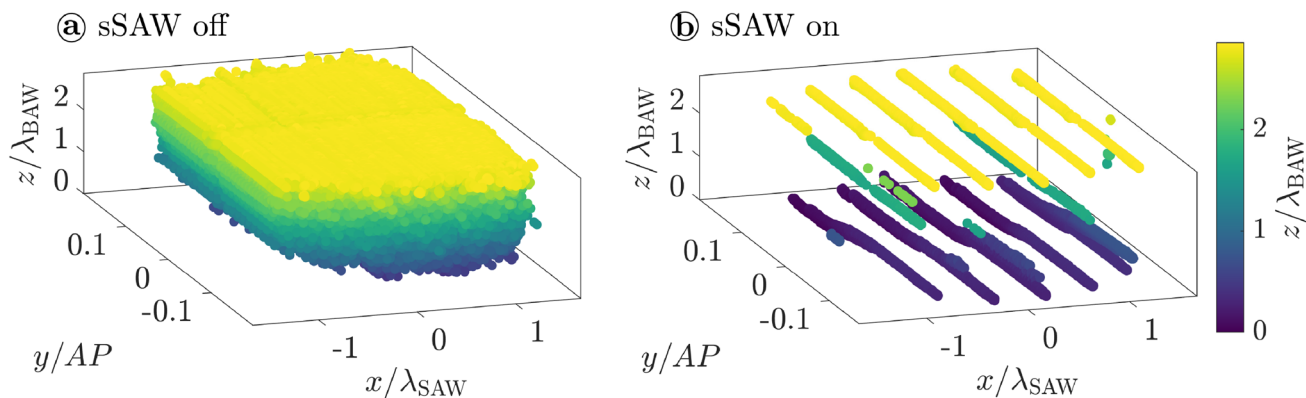


Fig. 5 Positions of detected spherical particles suspended in aqueous glycerol solution with $\rho_0 > \rho_p$ at a volume flow rate of $Q = 1 \mu\text{L min}^{-1}$ without (a) and with (b) the influence of the sSAW.

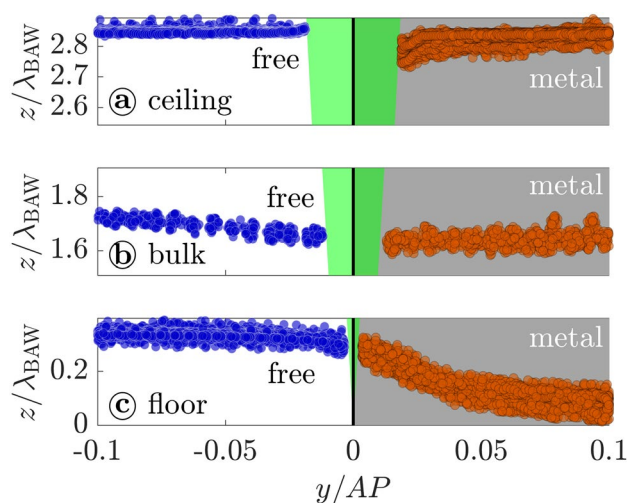


Fig. 6 Particle positions near the channel ceiling (a), the fluid bulk (b) and near the channel floor (c). Detected particles above the free and metallized substrate surface are shown in blue and orange, respectively. Shadowing effects occur in the area marked in green above the edge of the metal layer. To distinguish particles focused to stable locations, a nearest neighbour filter was applied. Please note that the scale of the abscissa in (c) also applies to (a, b) (color figure online)

were found near the channel floor ($z/\lambda_{BAW} < 0.5$) without the influence of the acoustoelectric wave field, this proportion increased to 46.5 % when the sSAW was activated. This phenomenon is strongly affected by the acoustically induced fluid flow, which is discussed below based on numerical simulations and in detail in our previous studies (Sachs et al. 2022a, b).

A detailed view on the detected particle positions in the three planes along the channel height is given in Fig. 6 at $x/\lambda_{SAW} \approx 0.6$. Due to shadowing effects at the edge of the metal layer, the particle image intensity varied in the green

The height position of the particles is encoded in the color. To distinguish particles focused to stable locations, a nearest neighbour filter was applied in (b) (color figure online)

marked area, resulting in a local increase of the measurement uncertainty. The particles found in this area were not considered in the following. While a comparable particle levitation of approx. $16.5\ \mu\text{m}$ occurred above the free substrate surface relative to the metallized region near the channel floor, no significant variation in the z -position was evident at higher planes. This observation indicates an influence of F_{DEP}^s only close to the substrate surface, which is negligible for particles in higher planes. The findings are in agreement with previous studies (Collins et al. 2014; Tayebi et al. 2021) and will further be analyzed numerically below.

Numerical simulation To shed light on the interplay of acoustic and dielectrophoretic forces in the manipulation of spherical particles, a three-dimensional numerical model has been set up. The calculated normalized amplitude \tilde{A} and time-averaged absolute electric potential $\langle |\phi| \rangle$ of the sSAW possess periodic structures with several nodes and antinodes that coincide along the channel width (see Fig. S7, SI). A metal layer was not considered in the numerical model, since the acoustic and dielectrophoretic effects can be evaluated independently. Furthermore, the dissipation of acoustic and electrical energy in the fluid, PDMS and LiNbO_3 substrate leads to local heating of the acoustofluidic device (Castellanos et al. 2003; Ha et al. 2015; Weser et al. 2022). As a result, the particle behavior might be affected by acoustothermal effects (Kondoh et al. 2005; Shilton et al. 2015; Das et al. 2019), which are beyond the scope of this study. However, since the effects of acoustic and dielectrophoretic forces on the particle behavior are examined relative to each other in the same acoustofluidic device, the experimental and numerical findings allow a thorough analysis of the interplay of both forces.

Based on the electric potential of the sSAW, closed field lines of the electric field are formed between two neighboring antinodes of the sSAW as depicted in Fig. 7a for half the channel cross-section. The magnitude of the electric field maximizes at the channel floor and decays exponentially in z -direction within the fluid. A spherical polystyrene particle in this non-uniform electric field experiences a negative DEP force according to Eq. (14). The resulting force potential $\tilde{\xi}$ is depicted in Fig. 7a after normalization by its maximum. In addition, vectors indicate the direction of F_{DEP}^s . Due to the quadratic dependence $\xi \propto |E|^2$ on the electric field, ξ decays exponentially in z -direction. As a consequence of the strong gradients $\partial\xi/\partial z$ in z -direction, the force component $F_{\text{DEP},z}^s$ is consistently positive in the vicinity of the channel floor, i.e., the vectors always point away from the charged substrate surface. Simultaneously, only small gradients $\partial\xi/\partial x$ and force components $F_{\text{DEP},x}^s$ are present in x -direction. This is consistent with the experimentally observed lateral focusing

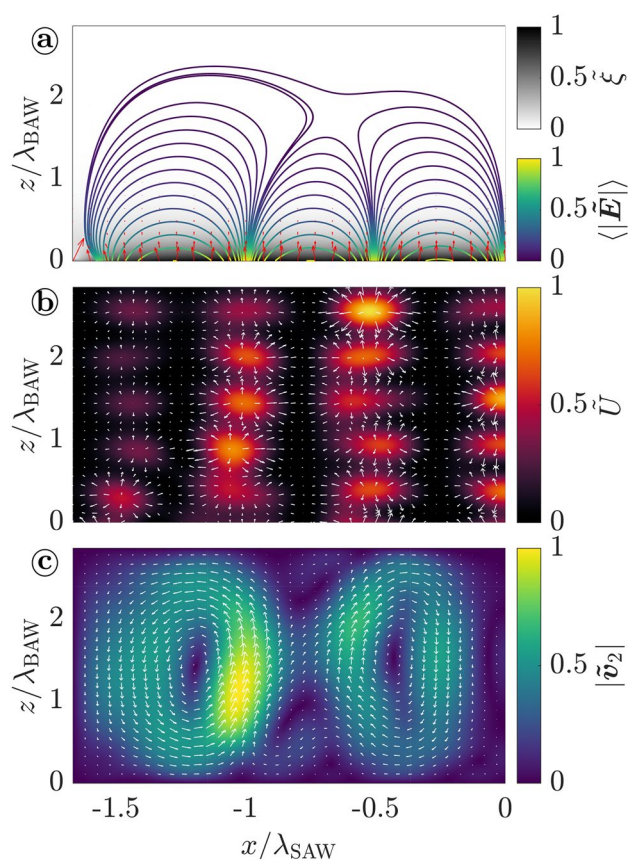


Fig. 7 Field lines of the normalized electric field, normalized dielectrophoretic force potential $\tilde{\xi}$ and vectors of F_{DEP}^s as a result of three-dimensional numerical simulations (a). The pattern of the normalized Gor'kov potential \tilde{U} with vectors of the acoustic radiation force is illustrated in (b). A stationary fluid flow is generated by damping of the BAWs in the fluid bulk (c). All fields are displayed in half the channel cross-section with a symmetry condition on the right side ($x/\lambda_{\text{SAW}} = 0$), corresponding to the channel centre. Please note that the scale of the abscissa in (c) also applies to (a, b)

of the particles dominated by acoustic forces, independent of the substrate surface coating.

In contrast to F_{DEP}^s , the pattern of the acoustic radiation force $F_{\text{RAD}}^s = -\nabla U$ comprises significant components in both the x - and z -directions across the entire channel cross-section as shown in Fig. 7b. Here, U denotes the time-averaged Gor'kov potential according to Eq. (18). The spatial pattern of the Gor'kov potential \tilde{U} (normalized with respect to its maximum) appears to be periodic both along the channel width (x -direction) due to the sSAW and along the channel height (z -direction) due to partial reflection of the acoustic waves at the channel ceiling. The resulting gradients in \tilde{U} lead to a spatial focusing of suspended particles on stable positions above the minima in \tilde{A} .

Furthermore, a stationary fluid flow is induced by attenuation of the BAWs in the fluid bulk (see Fig. 7c). In addition, a body force F_e appears due to inhomogeneities in the

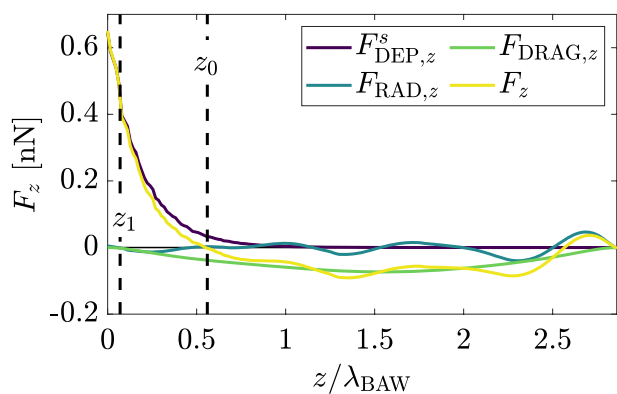


Fig. 8 Profiles of the z -component of the forces acting locally on a particle along a vertical line at $x/\lambda_{\text{SAW}} \approx -0.27$. The sum of all force components F_z undergoes several zero crossings with stable particle focus positions at z_0 and near the channel ceiling. If $F_{\text{DEP},z}^s$ is neglected, a new stable particle position is obtained at z_1 near the channel floor (color figure online)

electric field, scaling with $\nabla \times (\mathbf{E} \times \mathbf{E}^*)$. However, since \mathbf{F}_e decays rapidly in z -direction, the influence of this body force on the induced fluid flow is negligible if the channel height is greater than half the wavelength of the BAW and $128^\circ \text{YX LiNbO}_3$ is used as substrate (Darinskii et al. 2018; Dietzel and Hardt 2020). A suspended particle experiences Stokes’ drag \mathbf{F}_{DRAG} as a function of the velocity difference between the particle velocity \mathbf{u}_p and the fluid velocity \mathbf{v}_2 .

In Fig. 8, the z -components of all forces acting in a well of the Gor’kov potential ($x/\lambda_{\text{SAW}} \approx -0.27$) are plotted along the channel height. The particles are pushed to stable positions of force equilibrium. Since the particles are not in motion when occupying these positions, the particle velocity was set $\mathbf{u}_p \equiv 0$ to calculate $F_{\text{DRAG},z}$. As expected, the DEP force component $F_{\text{DEP},z}^s$ decreases exponentially with z and consistently takes positive values as CM' is negative. In contrast, $F_{\text{RAD},z}$ appears to be periodic and $F_{\text{DRAG},z}$ takes negative values, since the fluid flow is directed downwards in the considered region. However, the sum $F_z = F_{\text{RAD},z} + F_{\text{DEP},z}^s + F_{\text{DRAG},z}$ is dominated by $F_{\text{DEP},z}^s$ for $z < \lambda_{\text{BAW}}/2$. Stable particle locations are found near the channel floor ($z/\lambda_{\text{BAW}} \approx 0.56$, marked as z_0) and ceiling. When the influence of $F_{\text{DEP},z}^s$ is strongly reduced, as was the case above the thin metal layer, the stable particle location is shifted downwards to z_1 close to the channel floor. However, the stable particle location in the vicinity of the channel ceiling remains unaffected. Similar behavior was demonstrated experimentally for particles entering the region above the metallized substrate surface and can consequently be attributed to the influence of $F_{\text{DEP},z}^s$.

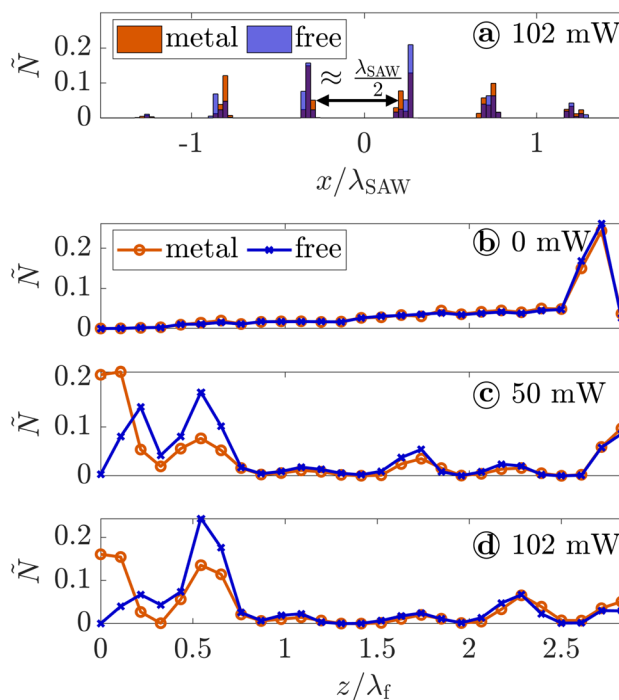


Fig. 9 Relative amount \tilde{N} of detected prolate spheroids in the region of free (orange) and metallized (blue) substrate surface. Detections close to the edge of the thin metal layer were not considered. The particle distribution at $P_{\text{el}} = 102 \text{ mW}$ is plotted in (a) along the channel width and in (d) along the channel height. The distribution across the z -coordinate is further depicted in (b) for $P_{\text{el}} = 0 \text{ mW}$ and in (c) for $P_{\text{el}} = 49.7 \text{ mW}$. In all measurements, the particles were suspended in a water-glycerine mixture (24 % v/v). Please note that the scale of the abscissa in (d) also applies to (b, c). Furthermore, the legend in (b) applies to (b–d)

3.3 Dynamical behavior of prolate spheroids

The position (x, y, z) and orientation (φ, θ) of prolate spheroids are key to reveal the interplay of acoustic and dielectrophoretic forces and torques in a standing acoustoelectric wave field. By analyzing fluorescence microscopy images, the in-plane positions (x, y) and orientations (φ) of particles suspended in a pressure-driven micro flow were obtained experimentally. The gained insights into the behavior of the non-spherical particles were subsequently used to model the interaction of the acoustoelectric wave field with a suspended particle in a three-dimensional numerical simulation.

Experiment The behavior of the particles is illustrated in video S1 (SI), while the distribution of particles detected in the micro channel with excitation of the sSAW is depicted in Fig. 9a along the channel width. The particles are focused on lines with invariant x -positions, having a distance of approx. $\lambda_{\text{SAW}}/2$. Analogous to the observed behavior of spherical particles (see Sect. 3.2), these stable focus locations are independent of the height position and metallization applied on the substrate surface. Hence, the experimental results

suggest that the lateral particle distribution is dominated by acoustic forces.

The entire channel height was covered by traversing the measurement volume stepwisely in z -direction. Since no APTV measurements were conducted for prolate spheroids, the relative number \tilde{N} of detected particles in the individual measurement planes indicates the particle distribution along the channel height. With the sSAW turned off, the number of detected particles increases with z (see Fig. 9b), as a water-glycerol mixture with a density greater than the density of the particles was used. The particle migration in vertical direction further leads to a considerable increase in the number of detections near the channel ceiling. When exciting the sSAW, the prolate spheroids are mainly found below $z/\lambda_{\text{BAW}} = 0.9$ as well as close to the channel ceiling (see Fig. 9c). However, several local maxima in $\tilde{N}(z)$ are evident in the fluid bulk, which indicate particles focused in stable locations. In the region of free substrate surface, two local peaks in $\tilde{N}(z)$ with almost the same number of detections are present at $z/\lambda_{\text{BAW}} \approx 0.22$ and 0.54 . However, the peak at the lower level disappears when the particles are located above the thin metal layer, while the majority of the detections occur in the vicinity of the channel floor. Furthermore, the relative frequency of detected particles at $z/\lambda_{\text{BAW}} = 0.54$ decreases. Consistent with the behavior of the spherical particles, the distribution of prolate spheroids remains unaffected above $z/\lambda_{\text{BAW}} = 0.9$.

By increasing the electrical power to $P_{\text{el}} \approx 102$ mW, the relative frequency of particles detected at $z/\lambda_{\text{BAW}} = 0.54$

rises in the region of free and metallized substrate surface. This might be caused by acoustothermal effects and acoustically induced vortex structures forming at the beginning of the sSAW field, which influence the initial particle positions (see Fig. S8, Sachs et al. 2022b). Both effects are more pronounced with increasing electrical power and potentially alter the preferred positions of the non-spherical particles. However, as these effects do not affect further evaluation of the relative influence of acoustophoresis and dielectrophoresis, a more in-depth analysis is considered for subsequent studies. Based on the experimental observations, it is reasonable to assume that the majority of the particles initially located below $z/\lambda_{\text{BAW}} = 0.33$ are pushed downwards when entering the region of metallized surface. As a result, a higher number of particles are still located near the channel floor. Simultaneously, a significant part of the particles initially located above $z/\lambda_{\text{BAW}} = 0.33$ seem to remain in a levitated position. As a result of the elongated shape of the particles, this levitated position remains stable due to acoustic forces, as discussed below based on numerical calculations.

In Fig. 10, the detected in-plane angle φ is shown at the free and metallized substrate surface in various measurement planes along the channel height. The vast majority of particles is oriented at an angle $\varphi \approx 180^\circ$, i.e., perpendicular to the minima in \tilde{A} (see Fig. S7), the channel side walls or the main flow direction (y -direction, see Fig. 2d). This orientation is consistent with observations in a shallower micro channel at comparable wavelength and electrical power of

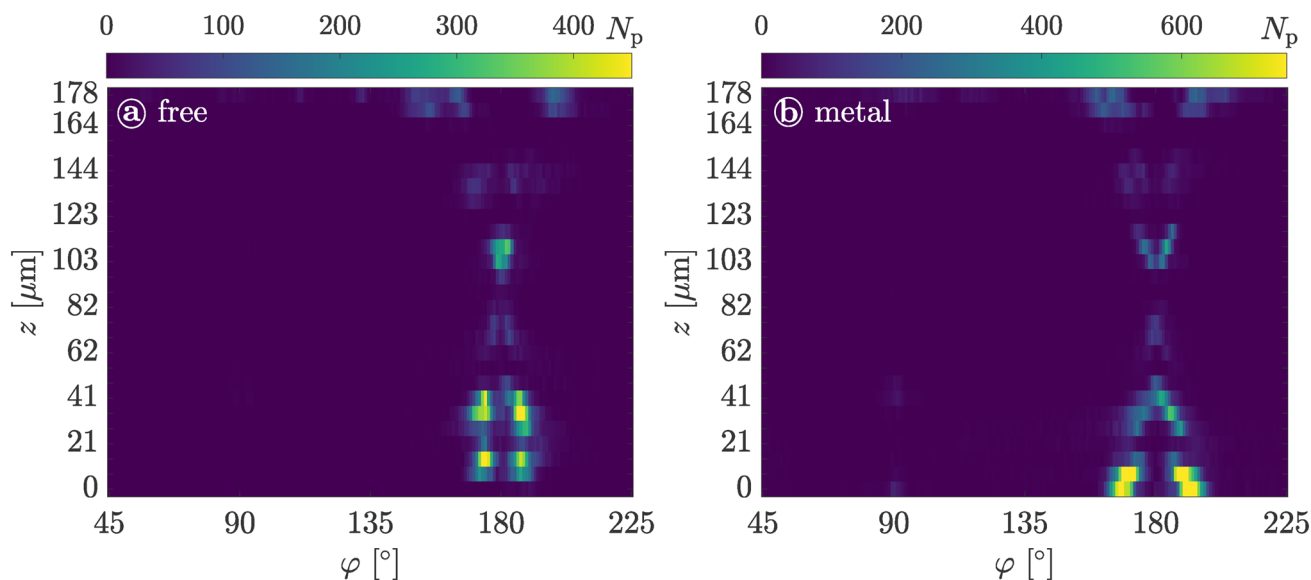


Fig. 10 Amount N_p of detected particles with in-plane angle φ along the channel height in the region of free (a) and metallized (b) substrate surface ($P_{\text{el}} = 49.7$ mW). Deviations from the preferred orientation at $\varphi = 180^\circ$ occur due to hydrodynamic torques towards

the channel bottom and channel top. However, these deviations are smaller in the region of free substrate surface near the channel bottom due to the effect of T_{DEP}

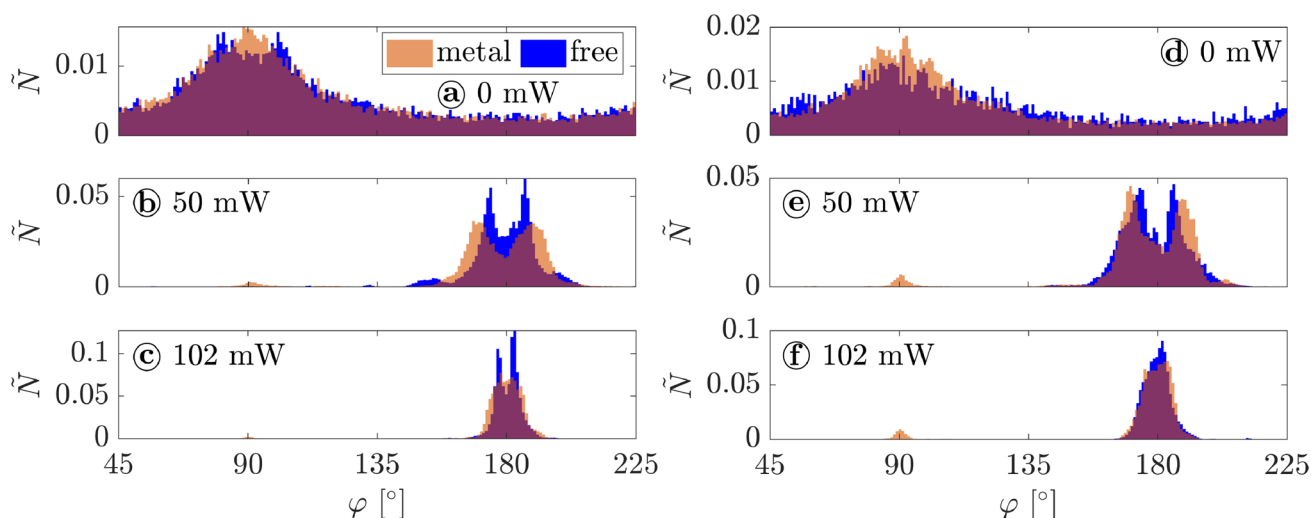


Fig. 11 Relative amount \tilde{N} of detected in-plane angles φ in a regular (a–c) and reversed (d–f) main flow. The electrical power P_{el} to excite

the sSAW amounted to 0 mW (a, d), 49.7 mW (b), 50.4 mW (e) and 102 mW (c, f). Please note that the scale of the abscissa in (c, f) also applies to (a, b, d, e). Furthermore, the legend in (a) applies to (a–f)

the sSAW (Sachs et al. 2023). Although the influence of the electric field decreases exponentially in z -direction, the orientation of the particles persists along the channel height both in the free and metallized substrate surface region. Thus, the experimental results suggest complementary effects of the dielectrophoretic T_{DEP} and acoustic torque T_{AC} . Velocity gradients in the main flow increase towards the floor and ceiling of the micro channel, exerting hydrodynamic torques on the particles. As a consequence, the in-plane angle deviates to a greater extent from $\varphi = 180^\circ$ in the vicinity of the channel floor and ceiling. However, the deviation from $\varphi = 180^\circ$ is less in the lower half of the channel in the region of free substrate surface than above the thin metal layer. This phenomenon is associated with the additional T_{DEP} acting near the channel floor, as discussed in more detail below.

The relative number \tilde{N} of detected in-plane angles φ is depicted in Fig. 11a–c for different level of electrical power P_{el} . In the absence of the sSAW, particles were preferentially oriented in main flow direction, i.e., $\varphi \approx 90^\circ$. Furthermore, the distribution of \tilde{N} is broader than under the influence of the acoustoelectric wave field due to transient particle motion (Lauricella et al. 2022; de Timary et al. 2022; Tai and Narsimhan 2022). The dielectrophoretic and acoustic torque impose a particle orientation of $\varphi \approx 180^\circ$, as shown in Fig. 11b, c. With increasing electrical power, the hydrodynamically caused deviation from $\varphi = 180^\circ$ and the proportion of particles oriented at 90° decrease. Due to the additional effect of T_{DEP} , the latter is significantly lower above the free substrate surface.

A similar trend exists when reversing the main flow direction as shown in Fig. 11d–f. However, the proportion of

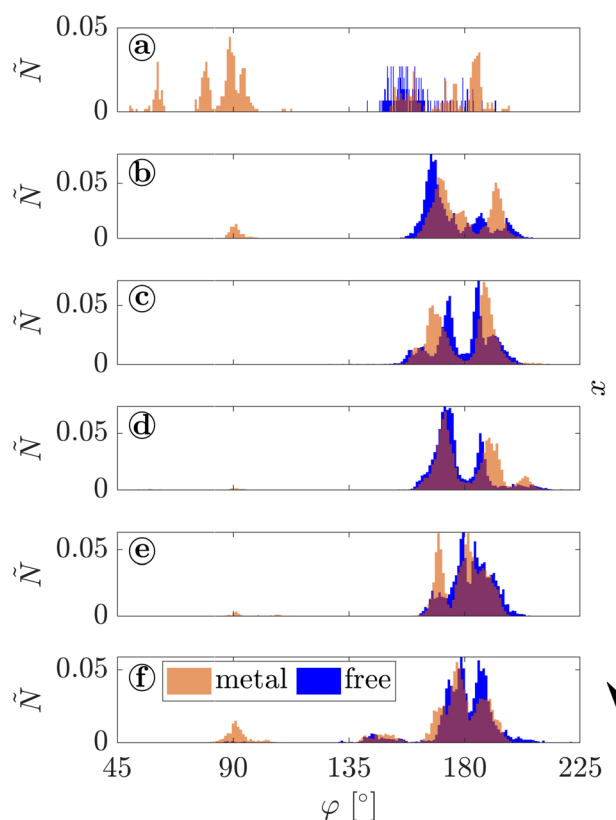


Fig. 12 Relative number \tilde{N} of detected in-plane angles φ in a reversed main flow in different focus locations along the channel width ($P_{el} = 50.4$ mW). The evaluation includes particles in $x/\lambda_{SAW} < -1.1$ (a), $x/\lambda_{SAW} \in [-1.1, -0.54]$ (b), $x/\lambda_{SAW} \in [-0.54, -0.11]$ (c), $x/\lambda_{SAW} \in [-0.11, 0.45]$ (d), $x/\lambda_{SAW} \in [0.45, 0.88]$ (e) and $x/\lambda_{SAW} > 0.88$ (f). Please note that the scale of the abscissa in (f) also applies to (a–e). Furthermore, the legend in (f) applies to (a–f)

particles at $\varphi \approx 90^\circ$ turns out to be larger. This observation is related to the initial orientation of the particles, which corresponds to the distribution without sSAW (see Fig. 11a) when the main flow direction is reversed. Hence, a stable particle orientation parallel to the minima in \tilde{A} ($\varphi = 90^\circ$) is observable based on the pattern of the acoustic field and under certain initial conditions. The relative number of detected φ is evaluated at stable particle locations along the channel width in Fig. 12 for $P_{\text{el}} = 50.4$ mW and reversed main flow. Particles at $\varphi \approx 90^\circ$ are preferably located near the channel side walls, where larger velocity gradients occur. Furthermore, the acoustically induced fluid flow (see Fig. 7c) is more pronounced in these regions due to travelling wave components of the sSAW. Both effects might influence the stable orientation of the particles and enhance the probability to find particles at $\varphi \approx 90^\circ$.

Numerical simulation To shed light on the acoustic and dielectrophoretic forces and torques on a non-spherical particle, the three-dimensional numerical model has been extended to include a prolate spheroid made of polystyrene. By numerically integrating the local forces and torques arising on the particle equilibrium surface S_0 , scattering effects of the BAWs, deflections of the acoustically induced fluid

flow and bending of field lines of the electric field were taken into account. In Fig. 13a, a prolate spheroid is depicted in a valley of the time-averaged absolute first-order pressure field $\langle |p_1| \rangle$ in half the channel cross-section. Besides the influence of the acoustic pressure field, the acoustically induced fluid flow affects the position and orientation of the particle through Stokes' drag as summarized in the acoustic force and torque according to Eqs. (21) and (23). Both the acoustic pressure field and the acoustically induced flow are influenced only locally by the suspended particle. The acoustic and hydrodynamic effects lead to a local force and torque distribution on the particle surface, as shown in Fig. 13c based on the normalized local x -component of the acoustic force $\tilde{F}_{\text{AC},l,x}$.

The position and orientation of the non-spherical particle is further affected by the pattern of the time-averaged absolute electric potential $\langle |\phi| \rangle$ and electric field E (see Fig. 13b). The field lines of the electric field extend between two antinodes of $\langle |p_1| \rangle$ in the fluid and converge in the piezoelectric substrate. However, in the vicinity of pressure nodes in $\langle |p_1| \rangle$, the field lines align almost horizontally. Due to the presence of a prolate spheroid with lower permittivity, the field lines are locally bent. Hence, a dielectrophoretic force

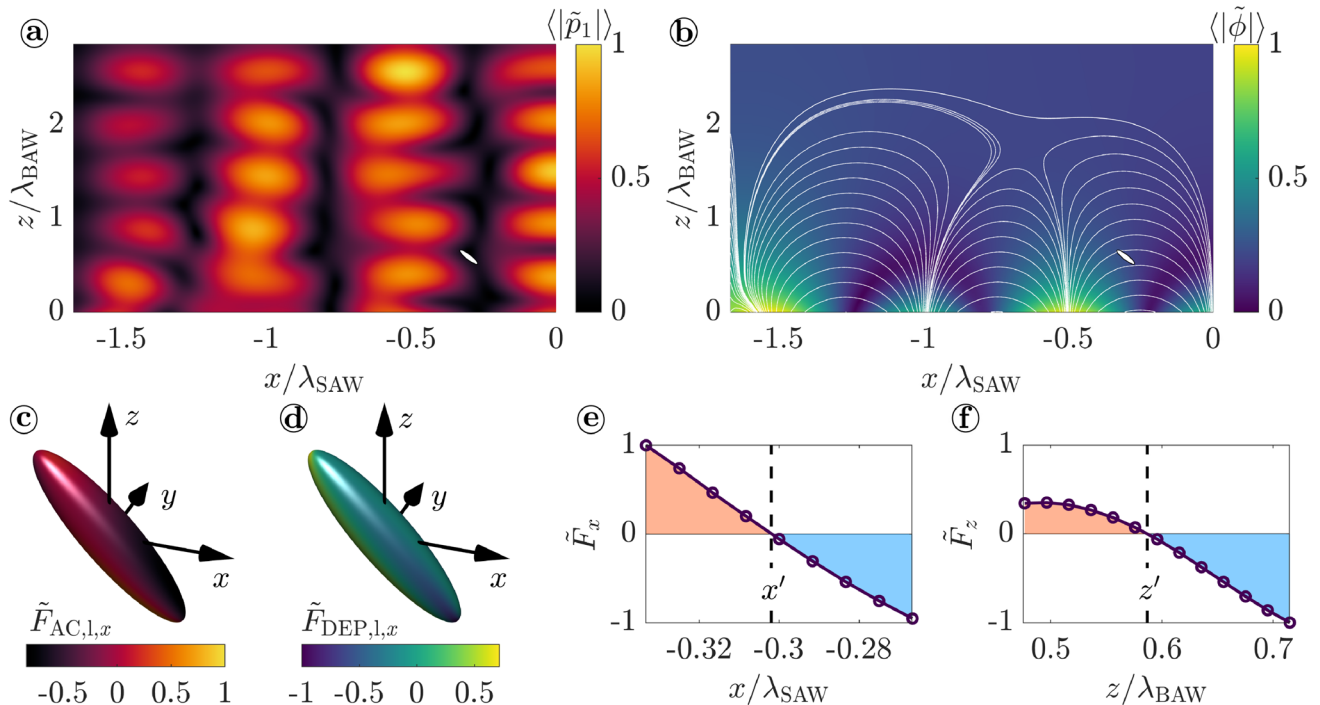


Fig. 13 Normalized time-averaged absolute first-order pressure field $\langle |\tilde{p}_1| \rangle$ (a) and normalized time-averaged absolute potential field $\langle |\tilde{\phi}| \rangle$ (b) obtained from numerical simulations. Field lines indicate the electric field E in (b) and a prolate spheroid was placed in a pressure node of $\langle |\tilde{p}_1| \rangle$. Please note that only half the channel cross section is depicted, while a symmetry condition was set at the right boundary,

which corresponds to the center of the channel. In (c, d), the distributions of the normalized local acoustic and dielectrophoretic force components ($\tilde{F}_{\text{AC},l,x}, \tilde{F}_{\text{DEP},l,x}$) on the particle surface are illustrated, respectively. The course of the normalized force components \tilde{F}_x and \tilde{F}_z for a displacement of prolate spheroids oriented at $\varphi = \theta = 0^\circ$ in x - and z -direction are shown in (e, f), respectively

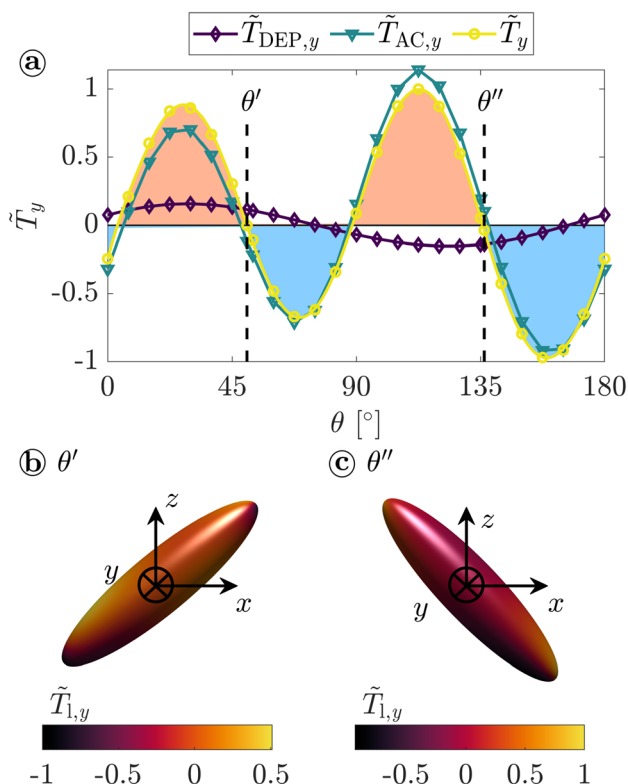


Fig. 14 Normalized torque about the y-axis \tilde{T}_y along with the acoustic and dielectrophoretic components ($\tilde{T}_{AC,y}$, $\tilde{T}_{DEP,y}$) as a function of the out-of-plane angle θ (a). The non-spherical particle was positioned at (x', y', z') and oriented with $\varphi = 0^\circ$. In (b, c), the normalized local torque component $\tilde{T}_{1,y}$ is plotted across the particle surface at the stable angles θ' and θ''

and torque exert on the particle. The normalized local distribution of the x-component $\tilde{F}_{DEP,x}$ on the particle surface is depicted in Fig. 13d.

Integration of the locally occurring forces across S_0 yields the total force $\mathbf{F} = \mathbf{F}_{AC} + \mathbf{F}_{DEP}$ acting on the particle. By evaluating the normalized force components in x- and z-direction, the stable focus position (x', z') of the particle in the channel cross-section at $y'/AP = -0.075$ can be derived. As indicated in Fig. 13e and f, both force components (F_x, F_z) cross the abscissa from positive to negative values. Hence, the particle is pushed to a stable location close to a local minimum of $\langle |p_1| \rangle$, which agrees well with experimental observations. Interestingly, the acoustic force component $F_{AC,z}$ also undergoes a zero crossing at $z/\lambda_{BAW} = 0.57$. Consequently, this explains the stable particle location in levitated height above the metallized substrate surface, as experimentally observed only for elongated particles.

To determine the stable orientation of the non-spherical particle located at (x', y', z') , the out-of-plane angle θ was varied in the range $[0^\circ, 180^\circ]$. The interplay of the y-components of the acoustic and dielectrophoretic torque is revealed in Fig. 14a. Both torque components

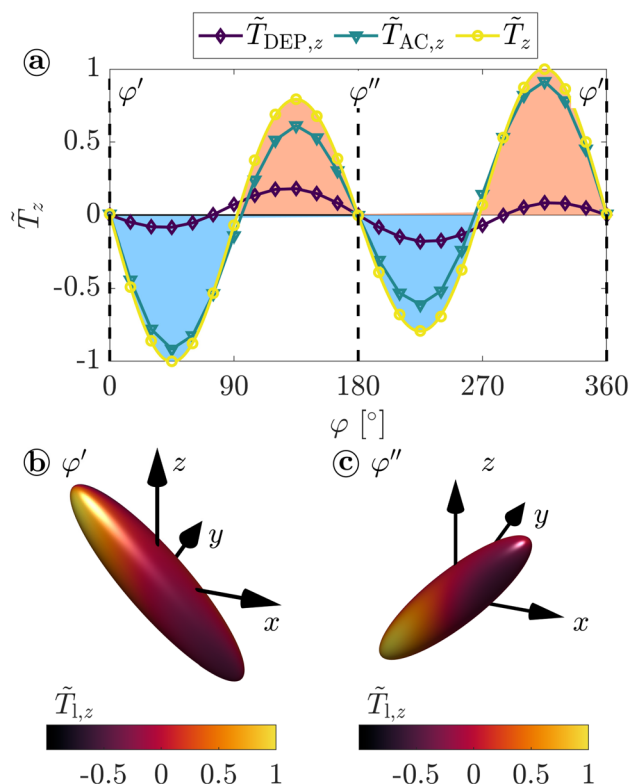


Fig. 15 Normalized torque components \tilde{T}_z , $\tilde{T}_{DEP,z}$ and $\tilde{T}_{AC,z}$ about the z-axis as a function of the in-plane angle φ (a). The prolate spheroid was positioned at (x', y', z') and oriented with θ'' . The distribution of the normalized local torque component $\tilde{T}_{1,z}$ across the particle surface is depicted for the stable in-plane angles φ' and φ'' in (b, c), respectively

possess periodic profiles as a function of θ with positive/negative regions in which the particle tends to rotate towards higher/lower θ , respectively. However, only one stable orientation is found based on $T_{DEP,y}$ as zero crossing at $\theta \approx 75^\circ$, while two stable orientations are possible according to $T_{AC,y}$. The sum of both torque components $T_y = T_{AC,y} + T_{DEP,y}$ reveals two stable out-of-plane angles θ' and θ'' . Both orientations are nearly perpendicular to each other as shown in Fig. 14b and c based on the normalized local torque distribution $\tilde{T}_{1,y}$ across the particle surface. Since $T_{AC,y}$ dominates over $T_{DEP,y}$ in the considered position (x', y', z') , the particle is primarily oriented in line with the pattern of the pressure node in $\langle |p_1| \rangle$ (see Fig. 13a). However, the relative dominance of one torque component is closely coupled to the pattern of the acoustic and electric fields and thus strongly depends on the spatial position of the particle. Although the out-of-plane angle cannot be determined in the experiments, an eccentric position of the maximum particle image intensity indicates an out-of-plane orientation (see Fig. S9, SI). Since this shift of the maximum particle image intensity occurs in positive and negative x-direction, it is reasonable to

assume that both stable out-of-plane angles (θ' , θ'') are occupied in the experiment.

With the stable out-of-plane orientation θ'' at hand, a successive in-plane rotation of the particle with $\varphi \in [0^\circ, 360^\circ]$ was performed. The resulting acoustic and dielectrophoretic torque components about the z -axis ($T_{AC,z}(\varphi)$, $T_{DEP,z}(\varphi)$) intersect the abscissa periodically with similar frequency as depicted in Fig. 15a. Furthermore, positive and negative regions overlap nearly entirely. Hence, complementary effects of the acoustic and dielectrophoretic torque exist on the in-plane orientation of the particle. Two stable particle orientations ($\varphi' = 0^\circ$ or 360° , $\varphi'' = 180^\circ$) emerge in the sum $T_z = T_{AC,z} + T_{DEP,z}$. However, since θ' and θ'' are almost perpendicular to each other, the orientation (φ'' , θ') resembles (φ' , θ'') as illustrated by the final orientation of the prolate spheroid in Fig. 15b and c. In addition, two unstable orientations at $\varphi \approx 90^\circ$ and 270° are revealed as zero crossings of $T_z(\varphi)$. However, small deviations from these orientations immediately lead to a rotation to φ' or φ'' .

The stable orientation at φ' and φ'' , i.e., perpendicular to the minima in \tilde{A} , is in excellent agreement with the experimental observations. Furthermore, the complementary progression of $T_{AC,z}(\varphi)$ and $T_{DEP,z}(\varphi)$ accounts for the preferred orientation of the particles at φ' and φ'' independent of the metal coating of the substrate surface and position of the particles along the channel height.

4 Conclusion

In this study, the interplay of acoustophoresis and dielectrophoresis was analyzed based on the behavior of spherical and non-spherical particles in an acoustoelectric wave field. To distinguish both phenomena in experiments, a thin metal layer was deposited on the surface of the piezoelectric lithium niobate substrate to screen the electric field. Analyzing spherical particles suspended in a pressure-driven micro channel flow shows that:

- The lateral focus positions of the particles remain unaffected by the electric field screening and are thus dominated by acoustophoresis.
- Particles with a negative real part of the Clausius-Mossotti factor located near the channel bottom are levitated by the dielectrophoretic force in the absence of the metal layer.
- At higher positions, the particles remain at a constant height level in both the region of free and metallized substrate surface. According to three-dimensional numerical simulations, this is related to the dielectrophoretic force decaying exponentially with the distance to the charged substrate surface.

Hence, regions along the channel height exist in microfluidic devices using surface acoustic waves in which particle height positions are primarily dominated by either acoustophoresis or dielectrophoresis.

The orientation of prolate spheroids is determined not only by the hydrodynamic torque due to the channel flow but also by the acoustic and dielectrophoretic torque. Experimental and numerical findings reveal that:

- The elongated particles prefer an orientation perpendicular to the pressure nodes of the pseudo-standing acoustic wave field, independent of their position along the channel height and screening of the electric field.
- The stable out-of-plane orientations of the particles are governed by the pattern of the acoustic pressure field in the vicinity of the pressure node analyzed numerically.
- Complementary effects of the acoustic and dielectrophoretic torque exist, which are consistent with the orientation of the particles independent of their z -position and the electric field screening in the experiment.
- Similar to the force distribution for spherical particles, the dielectrophoretic torque dominates in close vicinity to the substrate surface.

The symbiosis of experimental and numerical investigations shed light on the influence of the electric field on the particle behavior in a complex acoustoelectric wave field, which is inherently linked to the surface acoustic wave. By depositing thin metal layers on the substrate surface, the particle behavior can be manipulated systematically, which might drive innovative designs of acoustofluidic devices for particle concentration and separation.

Supplementary Information The online version contains supplementary material available at <https://doi.org/10.1007/s10404-024-02762-8>.

Acknowledgements The authors thank the German research foundation (DFG) for financial support within the priority program PP2045 “MehrDimPart” (444806275). Support by the Center of Micro- and Nanotechnologies (ZMN) (DFG RI sources reference: RI_00009), a DFG-funded core facility of TU Ilmenau is gratefully acknowledged. Furthermore, we thank Laura Weirauch (University of Bremen), who supported non-spherical particles. Technical support by Henning Schwabe using the high-performance computing cluster at the Universitätsrechenzentrum of TU Ilmenau is also gratefully acknowledged.

Author contributions S.S. contributed to conceptualization, data curation, formal analysis, investigation, methodology, software, validation, visualization, writing - original draft, and writing - review and editing. D.S. contributed to sample preparation, SEM measurements, and writing - review and editing. F.B. contributed to LDV measurements, and writing - review and editing. K.S.D. contributed to LDV measurements, resources, and writing - review and editing. C.C. contributed to conceptualization, methodology,

funding acquisition, project administration, resources, supervision, and writing - review and editing. J.K. contributed to conceptualization, methodology, LDV measurements, data evaluation, data curation, funding acquisition, project administration, resources, supervision, and writing - review and editing.

Funding Open Access funding enabled and organized by Projekt DEAL.

Data availability The full data sets that support the findings of this study are available from the corresponding author, S.S., upon request.

Declarations

Conflict of interest There are no conflicts to declare.

Ethical approval Not applicable.

Open Access This article is licensed under a Creative Commons Attribution 4.0 International License, which permits use, sharing, adaptation, distribution and reproduction in any medium or format, as long as you give appropriate credit to the original author(s) and the source, provide a link to the Creative Commons licence, and indicate if changes were made. The images or other third party material in this article are included in the article's Creative Commons licence, unless indicated otherwise in a credit line to the material. If material is not included in the article's Creative Commons licence and your intended use is not permitted by statutory regulation or exceeds the permitted use, you will need to obtain permission directly from the copyright holder. To view a copy of this licence, visit <http://creativecommons.org/licenses/by/4.0/>.

References

- Ahmed D, Mao X, Shi J, Juluri BK, Huang TJ (2009) A millisecond micromixer via single-bubble-based acoustic streaming. *Lab Chip* 9(18):2738–2741. <https://doi.org/10.1039/b903687c>
- Antfolk M, Magnusson C, Augustsson P, Lilja H, Laurell T (2015) Acoustofluidic, label-free separation and simultaneous concentration of rare tumor cells from white blood cells. *Anal Chem* 87(18):9322–9328. <https://doi.org/10.1021/acs.analchem.5b02023>
- Auld BA (1973) *Acoustic fields and waves in solids*, vol 1. Robert E. Krieger publishing company inc
- Bach JS, Bruus H (2018) Theory of pressure acoustics with viscous boundary layers and streaming in curved elastic cavities. *J Acoust Soc Am* 144(2):766. <https://doi.org/10.1121/1.5049579>
- Bach JS, Bruus H (2020) Suppression of acoustic streaming in shape-optimized channels. *Phys Rev Lett* 124(21):214501. <https://doi.org/10.1103/PhysRevLett.124.214501>
- Barnkob R, Nama N, Ren L, Huang TJ, Costanzo F, Kähler CJ (2018) Acoustically driven fluid and particle motion in confined and leaky systems. *Phys Rev Appl* 9(1):014027. <https://doi.org/10.1103/PhysRevApplied.9.014027>
- Barnkob R, Cierpka C, Chen M, Sachs S, Mäder P, Rossi M (2021) Defocus particle tracking: a comparison of methods based on model functions, cross-correlation, and neural networks. *Meas Sci Technol* 32(9):094011. <https://doi.org/10.1088/1361-6501/abfef6>
- Bernard I, Doinikov AA, Marmottant P, Rabaud D, Poulain C, Thibault P (2017) Controlled rotation and translation of spherical particles or living cells by surface acoustic waves. *Lab Chip* 17(14):2470–2480. <https://doi.org/10.1039/c7lc00084g>
- Bruus H (2012) Acoustofluidics 7: the acoustic radiation force on small particles. *Lab Chip* 12(6):1014–1021. <https://doi.org/10.1039/c2lc21068a>
- Bruus H (2012) Acoustofluidics 2: perturbation theory and ultrasound resonance modes. *Lab Chip* 12(1):20–28. <https://doi.org/10.1039/c1lc20770a>
- Castellanos A, Ramos A, González A, Green NG, Morgan H (2003) Electrohydrodynamics and dielectrophoresis in microsystems: scaling laws. *J Phys D Appl Phys* 36:2584–2597. <https://doi.org/10.1088/0022-3727/36/20/023>
- Çengel YA, Cimbala JM (2014) *Fluid mechanics: fundamentals and applications*, 3rd edn. McGraw Hill, New York
- Cheeke JDN (2002) *Fundamentals and applications of ultrasonic waves*. CRC series in pure and applied physics. CRC Press, Boca Raton
- Chen Y, Ding X, Steven Lin SC, Yang S, Huang PH, Nama N, Zhao Y, Nawaz AA, Guo F, Wang W, Gu Y, Mallouk TE, Huang TJ (2013) Tunable nanowire patterning using standing surface acoustic waves. *ACS Nano* 7(4):3306–3314. <https://doi.org/10.1021/nm4000034>
- Cierpka C, Segura R, Hain R, Kähler CJ (2010) A simple single camera 3C3D velocity measurement technique without errors due to depth of correlation and spatial averaging for microfluidics. *Meas Sci Technol* 21(4):045401. <https://doi.org/10.1088/0957-0233/21/4/045401>
- Cierpka C, Rossi M, Segura R, Kähler CJ (2011) On the calibration of astigmatism particle tracking velocimetry for microflows. *Meas Sci Technol* 22(1):015401. <https://doi.org/10.1088/0957-0233/22/1/015401>
- Cierpka C, Lütke B, Kähler CJ (2013) Higher order multi-frame particle tracking velocimetry. *Exp Fluids* 54(5):5. <https://doi.org/10.1007/s00348-013-1533-3>
- Collins DJ, Alan T, Neild A (2014) Particle separation using virtual deterministic lateral displacement (vDLD). *Lab Chip* 14(9):1595–1603. <https://doi.org/10.1039/c3lc51367j>
- Collins DJ, Ma Z, Ai Y (2016) Highly localized acoustic streaming and size-selective submicrometer particle concentration using high frequency microscale focused acoustic fields. *Anal Chem* 88(10):5513–5522. <https://doi.org/10.1021/acs.analchem.6b01069>
- Comsol multiphysics, version 6.1 (2024). <https://www.comsol.de/>
- Darinskii AN, Weihnacht M, Schmidt H (2018) Surface acoustic wave electric field effect on acoustic streaming: numerical analysis. *J Appl Phys* 123(1):014902. <https://doi.org/10.1063/1.5005849>
- Das PK, Snider AD, Bhethanabotla VR (2019) Acoustothermal heating in surface acoustic wave driven microchannel flow. *Phys Fluids* 31(10):106106. <https://doi.org/10.1063/1.5121307>
- de Lora JA, Auber mann F, Frey C, Jahnke T, Wang Y, Weber S, Platzman I, Spatz JP (2024) Evaluation of acoustophoretic and dielectrophoretic forces for droplet injection in droplet-based microfluidic devices. *ACS Omega* 9(14):16097–16105. <https://doi.org/10.1021/acsomega.3c09881>
- de Timary G, Rousseau CJ, van Melder en L, Scheid B (2022) Shear-enhanced sorting of ovoid and filamentous bacterial cells using pinch flow fractionation. *Lab Chip* 23(4):659–670. <https://doi.org/10.1039/d2lc00969b>
- Deng Z, Kondalkar VV, Cierpka C, Schmidt H, König J (2023) From rectangular to diamond shape: on the three-dimensional and size-dependent transformation of patterns formed by single particles trapped in microfluidic acoustic tweezers. *Lab Chip* 23(9):2154–2160. <https://doi.org/10.1039/d3lc00120b>
- Dietzel M, Hardt S (2020) Electroosmotic flow in small-scale channels induced by surface-acoustic waves. *Phys Rev Fluids* 5(12):123702. <https://doi.org/10.1103/PhysRevFluids.5.123702>
- Ding X, Li P, Lin SCS, Stratton ZS, Nama N, Guo F, Slotcavage D, Mao X, Shi J, Costanzo F, Huang TJ (2013) Surface acoustic

- wave microfluidics. *Lab Chip* 13(18):3626–3649. <https://doi.org/10.1039/c3lc50361e>
- Ding X, Peng Z, Lin SCS, Geri M, Li S, Li P, Chen Y, Dao M, Suresh S, Huang TJ (2014) Cell separation using tilted-angle standing surface acoustic waves. *Proc Natl Acad Sci USA* 111(36):12992–12997. <https://doi.org/10.1073/pnas.1413325111>
- Doinikov AA (1997) Acoustic radiation force on a spherical particle in a viscous heat-conducting fluid. I. General formula. *J Acoust Soc Am* 101(2):713–721. <https://doi.org/10.1121/1.418035>
- Dual J, Hahn P, Leibacher I, Möller D, Schwarz T, Wang J (2012) Acoustofluidics 19: ultrasonic microrobotics in cavities: devices and numerical simulation. *Lab Chip* 12(20):4010–4021. <https://doi.org/10.1039/c2lc40733g>
- Fakhfour A, Colditz M, Devendran C, Ivanova K, Jacob S, Neild A, Winkler A (2023) Fully microfabricated surface acoustic wave tweezer for collection of submicron particles and human blood cells. *ACS Appl Mater Interfaces*. <https://doi.org/10.1021/acsami.3c00537>
- Fan Z, Mei D, Yang K, Chen Z (2008) Acoustic radiation torque on an irregularly shaped scatterer in an arbitrary sound field. *J Acoust Soc Am* 124(5):2727–2732. <https://doi.org/10.1121/1.2977733>
- Fan Y, Wang X, Ren J, Lin F, Wu J (2022) Recent advances in acoustofluidic separation technology in biology. *Microsyst Nanoeng* 8:94. <https://doi.org/10.1038/s41378-022-00435-6>
- Farzam Rad V, Moradi AR (2020) Flat wall proximity effect on micro-particle sedimentation in non-Newtonian fluids. *Sci Rep* 10(1):2741. <https://doi.org/10.1038/s41598-020-59386-5>
- Franchini S, Krevor S (2020) Cut, overlap and locate: a deep learning approach for the 3D localization of particles in astigmatic optical setups. *Exp Fluids* 61(6):6. <https://doi.org/10.1007/s00348-020-02968-w>
- Gai J, Nosrati R, Neild A (2020) High DNA integrity sperm selection using surface acoustic waves. *Lab Chip* 20(22):4262–4272. <https://doi.org/10.1039/d0lc00457j>
- Gao Y, Wu M, Lin Y, Xu J (2020) Acoustic microfluidic separation techniques and bioapplications: a review. *Micromachines* 11(10):921. <https://doi.org/10.3390/mi11100921>
- Ghayour R, Hoojat Y, Karafi MR, Sadeghiyan H (2018) Development of a hybrid dep-saw device for trapping/sensing target cells. *Appl Acoust* 141:355–361. <https://doi.org/10.1016/j.apacoust.2018.07.028>
- Giesler J, Weirauch L, Pesch GR, Baune M, Thöming J (2023) Semi-continuous dielectrophoretic separation at high throughput using printed circuit boards. *Sci Rep* 13(1):20696. <https://doi.org/10.1038/s41598-023-47571-1>
- Gossett DR, Weaver WM, Mach AJ, Hur SC, Tse HTK, Lee W, Amini H, Di Carlo D (2010) Label-free cell separation and sorting in microfluidic systems. *Anal Bioanal Chem* 397(8):3249–3267. <https://doi.org/10.1007/s00216-010-3721-9>
- Ha BH, Lee KS, Destgeer G, Park J, Choung JS, Jung JH, Shin JH, Sung HJ (2015) Acoustothermal heating of polydimethylsiloxane microfluidic system. *Sci Rep* 5:11851. <https://doi.org/10.1038/srep11851>
- Hettiarachchi S, Cha H, Ouyang L, Mudugamuwa A, An H, Kijanka G, Kashaninejad N, Nguyen NT, Zhang J (2022) Recent microfluidic advances in submicron to nanoparticle manipulation and separation. *Lab Chip*. <https://doi.org/10.1039/d2lc00793b>
- Hoque SZ, Bhattacharyya K, Sen AK (2022) Dynamical motion of an oblate shaped particle exposed to an acoustic standing wave in a microchannel. *Phys Rev Fluids* 7(11):11. <https://doi.org/10.1103/PhysRevFluids.7.114204>
- Hsu JC, Chao CL (2020) Full-wave modeling of micro-acoustofluidic devices driven by standing surface acoustic waves for micro-particle acoustophoresis. *J Appl Phys* 128(12):124502. <https://doi.org/10.1063/5.0017933>
- Jiang D, Liu J, Pan Y, Zhuang L, Wang P (2021) Surface acoustic wave (saw) techniques in tissue engineering. *Cell Tissue Res* 386(2):215–226. <https://doi.org/10.1007/s00441-020-03397-1>
- Joergensen JH (2022) Theory and modeling of thermoviscous acoustofluidics. Ph.D. thesis, Technical University of Denmark, Lyngby
- Joergensen JH, Bruus H (2021) Theory of pressure acoustics with thermoviscous boundary layers and streaming in elastic cavities. *J Acoust Soc Am* 149(5):3599. <https://doi.org/10.1121/10.0005005>
- Johnson DA, Feke DL (1995) Methodology for fractionating suspended particles using ultrasonic standing wave and divided flow fields. *Sep Technol* 5:251–258. [https://doi.org/10.1016/0956-9618\(95\)00130-1](https://doi.org/10.1016/0956-9618(95)00130-1)
- Kähler CJ, Scharnowski S, Cierpka C (2012) On the uncertainty of digital PIV and PTV near walls. *Exp Fluids* 52(6):1641–1656. <https://doi.org/10.1007/s00348-012-1307-3>
- Karlsen JT (2018) Theory of nonlinear acoustic forces acting on fluid and particles in microsystems. Ph.D. thesis, Technical University of Denmark, Lyngby
- Khan MS, Ali M, Lee SH, Jang KY, Lee SJ, Park J (2024) Acoustofluidic separation of prolate and spherical micro-objects. *Microsyst Nanoeng* 10(6):6. <https://doi.org/10.1038/s41378-023-00636-7>
- Kiebert F, Wege S, Massing J, König J, Cierpka C, Weser R, Schmidt H (2017) 3D measurement and simulation of surface acoustic wave driven fluid motion: a comparison. *Lab Chip* 17(12):2104–2114. <https://doi.org/10.1039/c7lc00184c>
- King LV (1934) On the acoustic radiation pressure on spheres. *Proc R Soc Lond Ser A Math Phys Sci* 147(861):212–240. <https://doi.org/10.1098/rspa.1934.0215>
- Kondoh J, Shimizu N, Matsui Y, Shiokawa S (2005) Liquid heating effects by saw streaming on the piezoelectric substrate. *IEEE Trans Ultrason Ferroelectr Freq Control* 52(10):1881–1883. <https://doi.org/10.1109/tuffc.2005.1561646>
- Kong XH, Deneke C, Schmidt H, Thurmer DJ, Bauer M, Schmidt OG (2010) Surface acoustic wave mediated dielectrophoretic alignment of rolled-up microtubes in microfluidic systems. *Appl Phys Lett* 96(13):134105. <https://doi.org/10.1063/1.3371708>
- König J, Chen M, Rösing W, Boho D, Mäder P, Cierpka C (2020) On the use of a cascaded convolutional neural network for three-dimensional flow measurements using astigmatic PTV. *Meas Sci Technol* 31(7):074015. <https://doi.org/10.1088/1361-6501/ab7bfd>
- Laurell T, Petersson F, Nilsson A (2007) Chip integrated strategies for acoustic separation and manipulation of cells and particles. *Chem Soc Rev* 36(3):492–506. <https://doi.org/10.1039/b601326k>
- Lauricella G, Zhou J, Luan Q, Papautsky I, Peng Z (2022) Computational study of inertial migration of prolate particles in a straight rectangular channel. *Phys Fluids* 34(8):082021. <https://doi.org/10.1063/5.0100963>
- Leibacher I, Reichert P, Dual J (2015) Microfluidic droplet handling by bulk acoustic wave (BAW) acoustophoresis. *Lab Chip* 15(13):2896–2905. <https://doi.org/10.1039/c5lc00083a>
- Li P, Mao Z, Peng Z, Zhou L, Chen Y, Huang PH, Truica CI, Drabick JJ, El-Deiry WS, Dao M, Suresh S, Huang TJ (2015) Acoustic separation of circulating tumor cells. *Proc Natl Acad Sci USA* 112(16):4970–4975. <https://doi.org/10.1073/pnas.1504484112>
- Liu G, He F, Li X, Zhao H, Zhang Y, Li Z, Yang Z (2019) Multi-level separation of particles using acoustic radiation force and hydraulic force in a microfluidic chip. *Microfluid Nanofluid* 23(2):23. <https://doi.org/10.1007/s10404-019-2189-y>
- Ma Z, Guo J, Liu YJ, Ai Y (2015) The patterning mechanism of carbon nanotubes using surface acoustic waves: the acoustic radiation effect or the dielectrophoretic effect. *Nanoscale* 7(33):14047–14054. <https://doi.org/10.1039/c5nr04272k>
- Miyagawa A, Okada T (2021) Particle manipulation with external field; from recent advancement to perspectives. *Anal Sci* 37(1):69–78. <https://doi.org/10.2116/analsci.20SAR03>

- Morgan H, Green NG (2003) AC electrokinetics: colloids and nanoparticles, vol 2. Research Studies Press, Baldock
- Nam J, Lim H, Kim D, Shin S (2011) Separation of platelets from whole blood using standing surface acoustic waves in a microchannel. *Lab Chip* 11(19):3361–3364. <https://doi.org/10.1039/c1lc20346k>
- Nam J, Lee Y, Shin S (2011) Size-dependent microparticles separation through standing surface acoustic waves. *Microfluid Nanofluid* 11:317–326. <https://doi.org/10.1007/s10404-011-0798-1>
- Nasiri R, Shamloo A, Ahadian S, Amirifar L, Akbari J, Goudie MJ, Lee K, Ashammakhi N, Dokmeci MR, Di Carlo D, Khademhosseini A (2020) Microfluidic-based approaches in targeted cell/particle separation based on physical properties: fundamentals and applications. *Small* 16(29):e2000171. <https://doi.org/10.1002/sml.202000171>
- Nili H, Sun T, Green NG (2011) Higher order dielectrophoretic force characterisation of non-spherical particles. In: 13th international conference on electrostatics, vol 301, p 012061
- Nyborg WL (1953) Acoustic streaming due to attenuated plane waves. *J Acoust Soc Am* 25(1):68–75. <https://doi.org/10.1121/1.1907010>
- Pohl HA, Crane JS (1972) Dielectrophoretic force. *J Theor Biol* 37(1):1–13. [https://doi.org/10.1016/0022-5193\(72\)90112-9](https://doi.org/10.1016/0022-5193(72)90112-9)
- Ratz M, Sachs S, König J, Cierpka C (2023) A deep neural network architecture for reliable 3D position and size determination for Lagrangian particle tracking using a single camera. *Meas Sci Technol* 34(10):105203. <https://doi.org/10.1088/1361-6501/ace070>
- Riaud A, Baudoin M, Bou Matar O, Thomas JL, Brunet P (2017) On the influence of viscosity and caustics on acoustic streaming in sessile droplets: an experimental and a numerical study with a cost-effective method. *J Fluid Mech* 821:384–420. <https://doi.org/10.1017/jfm.2017.178>
- Riccardi M, Martin OJF (2023) Electromagnetic forces and torques: from dielectrophoresis to optical tweezers. *Chem Rev* 123(4):1680–1711. <https://doi.org/10.1021/acs.chemrev.2c00576>
- Richard C, Fakhfour A, Colditz M, Striggow F, Kronstein-Wiedemann R, Tonn T, Medina-Sánchez M, Schmidt OG, Gemming T, Winkler A (2019) Blood platelet enrichment in mass-producible surface acoustic wave (SAW) driven microfluidic chips. *Lab Chip* 19(24):4043–4051. <https://doi.org/10.1039/c9lc00804g>
- Sachs S, Baloochi M, Cierpka C, König J (2022a) On the acoustically induced fluid flow in particle separation systems employing standing surface acoustic waves—part I. *Lab Chip* 22(10):2011–2027. <https://doi.org/10.1039/d1lc01113h>
- Sachs S, Cierpka C, König J (2022b) On the acoustically induced fluid flow in particle separation systems employing standing surface acoustic waves—part II. *Lab Chip* 22(10):2028–2040. <https://doi.org/10.1039/d2lc00106c>
- Sachs S, Schmidt H, Cierpka C, König J (2023) On the behavior of prolate spheroids in a standing surface acoustic wave field. *Microfluid Nanofluid* 27:81. <https://doi.org/10.1007/s10404-023-02690-z>
- Sachs S, Ratz M, Mäder P, König J, Cierpka C (2023) Particle detection and size recognition based on defocused particle images: a comparison of a deterministic algorithm and a deep neural network. *Exp Fluids* 64(21):21. <https://doi.org/10.1007/s00348-023-03574-2>
- Sajeesh P, Sen AK (2014) Particle separation and sorting in microfluidic devices: a review. *Microfluid Nanofluid* 17(1):1–52. <https://doi.org/10.1007/s10404-013-1291-9>
- Seemann KM, Ebbecke J, Wixforth A (2006) Alignment of carbon nanotubes on pre-structured silicon by surface acoustic waves. *Nanotechnology* 17(17):4529–4532. <https://doi.org/10.1088/0957-4484/17/17/040>
- Settnes M, Bruus H (2012) Forces acting on a small particle in an acoustical field in a viscous fluid. *Phys Rev E Stat Nonlinear Soft Matter Phys* 85(1 Pt 2):016327. <https://doi.org/10.1103/PhysRevE.85.016327>
- Shi J, Ahmed D, Mao X, Lin SCS, Lawit A, Huang TJ (2009) Acoustic tweezers: patterning cells and microparticles using standing surface acoustic waves (SSAW). *Lab Chip* 9(20):2890–2895. <https://doi.org/10.1039/b910595f>
- Shilton R, Tan MK, Yeo LY, Friend JR (2008) Particle concentration and mixing in microdrops driven by focused surface acoustic waves. *J Appl Phys* 104(1):014910. <https://doi.org/10.1063/1.2951467>
- Shilton RJ, Mattoli V, Travagliati M, Agostini M, Desii A, Beltram F, Cecchini M (2015) Rapid and controllable digital microfluidic heating by surface acoustic waves. *Adv Funct Mater* 25(37):5895–5901. <https://doi.org/10.1002/adfm.201501130>
- Silva GT, Lobo TP, Mitri FG (2012) Radiation torque produced by an arbitrary acoustic wave. *EPL (Europhys Lett)* 97(5):54003. <https://doi.org/10.1209/0295-5075/97/54003>
- Skov NR, Bruus H (2016) Modeling of microdevices for saw-based acoustophoresis—a study of boundary conditions. *Micromachines* 7(10):182. <https://doi.org/10.3390/mi7100182>
- Strobl CJ, Schäfflein C, Beierlein U, Ebbecke J, Wixforth A (2004) Carbon nanotube alignment by surface acoustic waves. *Appl Phys Lett* 85(8):1427–1429. <https://doi.org/10.1063/1.1787159>
- Tai CW, Narsimhan V (2022) Experimental and theoretical studies of cross-stream migration of non-spherical particles in a quadratic flow of a viscoelastic fluid. *Soft Matter* 18(24):4613–4624. <https://doi.org/10.1039/d2sm00011c>
- Tayebi M, Yang D, Collins DJ, Ai Y (2021) Deterministic sorting of submicrometer particles and extracellular vesicles using a combined electric and acoustic field. *Nano Lett* 21(16):6835–6842. <https://doi.org/10.1021/acs.nanolett.1c01827>
- Tian Z, Wang Z, Zhang P, Naquin TD, Mai J, Wu Y, Yang S, Gu Y, Bachman H, Liang Y, Yu Z, Jun HT (2020) Generating multifunctional acoustic tweezers in petri dishes for contactless, precise manipulation of bioparticles. *Sci Adv* 6(37):eabb0494
- Wang X, Wang XB, Gascoyne PR (1997) General expressions for dielectrophoretic force and electrorotational torque derived using the Maxwell stress tensor method. *J Electrostat* 39:277–295. [https://doi.org/10.1016/S0304-3886\(97\)00126-5](https://doi.org/10.1016/S0304-3886(97)00126-5)
- Weirauch L, Giesler J, Baune M, Pesch GR, Thöming J (2022) Shape-selective remobilization of microparticles in a mesh-based dep filter at high throughput. *Sep Purif Technol* 300:121792. <https://doi.org/10.1016/j.seppur.2022.121792>
- Weser R, Winkler A, Weihnacht M, Menzel S, Schmidt H (2020) The complexity of surface acoustic wave fields used for microfluidic applications. *Ultrasonics* 106:106160. <https://doi.org/10.1016/j.ultras.2020.106160>
- Weser R, Deng Z, Kondalkar VV, Darinskii AN, Cierpka C, Schmidt H, König J (2022) Three-dimensional heating and patterning dynamics of particles in microscale acoustic tweezers. *Lab Chip* 22(15):2886–2901. <https://doi.org/10.1039/d2lc00200k>
- Wiklund M (2012) Acoustofluidics 12: biocompatibility and cell viability in microfluidic acoustic resonators. *Lab Chip* 12(11):2018–2028. <https://doi.org/10.1039/c2lc40201g>
- Wu M, Ouyang Y, Wang Z, Zhang R, Huang PH, Chen C, Li H, Li P, Quinn D, Dao M, Suresh S, Sadovsky Y, Huang TJ (2017) Isolation of exosomes from whole blood by integrating acoustics and microfluidics. *Proc Natl Acad Sci USA* 114(40):10584–10589. <https://doi.org/10.1073/pnas.1709210114>
- Wu M, Mao Z, Chen K, Bachman H, Chen Y, Rufo J, Ren L, Li P, Wang L, Huang TJ (2017) Acoustic separation of nanoparticles in continuous flow. *Adv Funct Mater* 27(14):1606039. <https://doi.org/10.1002/adfm.201606039>
- Wu M, Huang PH, Zhang R, Mao Z, Chen C, Kemeny G, Li P, Lee AV, Gyanchandani R, Armstrong AJ, Dao M, Suresh S, Huang TJ (2018) Circulating tumor cell phenotyping via high-throughput acoustic separation. *Small* 14(32):e1801131. <https://doi.org/10.1002/sml.201801131>

- Yazdi AA, D'Avino G (2023) Sedimentation and migration dynamics of a spherical particle in an elastoviscoplastic fluid near a wall. *J Nonnewton Fluid Mech* 314:105004. <https://doi.org/10.1016/j.jnnfm.2023.105004>
- Yeo LY, Friend JR (2014) Surface acoustic wave microfluidics. *Annu Rev Fluid Mech* 46(1):379–406. <https://doi.org/10.1146/annurev-fluid-010313-141418>
- Zeng Q, Guo F, Yao L, Zhu HW, Zheng L, Guo ZX, Liu W, Chen Y, Guo SS, Zhao XZ (2011) Milliseconds mixing in microfluidic channel using focused surface acoustic wave. *Sens Actuators B Chem* 160(1):1552–1556. <https://doi.org/10.1016/j.snb.2011.08.075>
- Zeng Q, Li L, Ma HL, Xu J, Fan Y, Wang H (2013) A non-contact strategy for controlled enrichment, manipulation, and separation of carbon nanotubes by surface acoustic waves. *Appl Phys Lett* 102(21):21. <https://doi.org/10.1063/1.4807677>
- Zhang S, Wang Y, Onck P, den Toonder J (2020) A concise review of microfluidic particle manipulation methods. *Microfluid Nano-fluid* 24(4):4. <https://doi.org/10.1007/s10404-020-2328-5>
- Zhang P, Rufo J, Chen C, Xia J, Tian Z, Zhang L, Hao N, Zhong Z, Gu Y, Chakrabarty K, Huang TJ (2021) Acoustoelectronic nanotweezers enable dynamic and large-scale control of nanomaterials. *Nat Commun* 12(1):3844. <https://doi.org/10.1038/s41467-021-24101-z>
- Zhao S, Wu M, Yang S, Wu Y, Gu Y, Chen C, Ye J, Xie Z, Tian Z, Bachman H, Huang PH, Xia J, Zhang P, Zhang H, Huang TJ (2020) A disposable acoustofluidic chip for nano/microparticle separation using unidirectional acoustic transducers. *Lab Chip* 20(7):1298–1308. <https://doi.org/10.1039/d0lc00106f>
- Zheng T, Wang C, Xu C (2020) Tritoroidal particle rings formation in open microfluidics induced by standing surface acoustic waves. *Electrophoresis* 41(10–11):983–990. <https://doi.org/10.1002/elps.201900361>

Publisher's Note Springer Nature remains neutral with regard to jurisdictional claims in published maps and institutional affiliations.